UNIVERSITY OF SOUTHAMPTON
FACULTY OF ENGINEERING, SCIENCE & MATHEMATICS
SCHOOL OF PHYSICS & ASTRONOMY

A Study of Auroral Fine Structure in the Magnetic Zenith

Daniel Keith Whiter

SUBMITTED FOR THE DEGREE OF
MASTER OF PHILOSOPHY

March 2008

UNIVERSITY OF SOUTHAMPTON

ABSTRACT

FACULTY OF ENGINEERING, SCIENCE & MATHEMATICS
SCHOOL OF PHYSICS & ASTRONOMY

Master of Philosophy

A STUDY OF AURORAL FINE STRUCTURE IN THE MAGNETIC ZENITH

by Daniel Keith Whiter

An auroral event which occurred over Spitsbergen at 17:25–17:30 UT on 26 January 2006 has been studied in detail. The instruments used to study the event include a high resolution echelle spectrograph, a white light television camera, photometers, and the EISCAT incoherent scatter radar.

It is usually assumed that the magnetic zenith is fixed in a constant point above the observer when studying auroral data. By analysing rayed coronal aurora an accurate position for the magnetic zenith was found for portions of the event studied here. It was found that this auroral zenith moved by approximately 2 degrees on timescales of a few seconds. At times it moved outside of the main beam of the EISCAT radar entirely.

The structure of the aurora within the region of the magnetic zenith was studied over the different stages of the event. By considering the auroral structure many features of the data recorded by the various instruments have been explained. This shows how important it is to use a variety of data inputs when studying the ionosphere. Auroral modelling of the 732.0 nm O^+ line and F-region electron densities showed that it is important to consider contributions to the electron density from field lines which are not entirely within the field of view of the radar.

In addition to the study of the 26 January 2006 event a new method for intensity calibrating a low-light spectrograph has been demonstrated and verified. This new method uses the measurements made of stars during a normal data run. It provides a good calibration with many advantages over the method employed in the past for calibration of the spectrograph used here.

Contents

List of Figures 4

List of Tables 6

Declaration of Authorship 7

Acknowledgements 8

1 Introduction 10

1.1 Theoretical background 12

1.1.1 The aurora 12

1.1.2 The ionosphere 13

1.1.3 Auroral emissions used in this study 13

2 Instrumentation 17

2.1 The Spectrographic Imaging Facility 17

2.1.1 HiTIES 19

2.1.2 TLC 21

2.1.3 Photometers 23

2.2 EISCAT 24

3 Absolute Intensity Calibration of the HiTIES Spectrograph 26

3.1 Aim of intensity calibration 26

3.2 Initial intensity calibration 26

3.3 Absolute intensity calibration using stars 29

3.4 Calculating theoretical star fluxes 33

3.5 Comparison between star and lamp based calibration methods . 35

4 Short Term Changes in the Position of the Magnetic Zenith 37
4.1 What is the magnetic zenith? 37
4.2 Locating the magnetic zenith in camera data 38
4.3 Finding the magnetic zenith from a field model 40
4.4 Analysis and results 44

5 Spectrograph, Photometer and EISCAT Data 51
5.1 HiTIES data 51
5.2 Photometer data 55
5.3 ESR data 58
5.4 Summary of data 60
5.5 Link between magnetic zenith motion and photometer data? . . 61

6 Modelling and Interpretation 63
6.1 The ion chemistry and electron transport model 63
6.1.1 Calculating the model 7320 Å emission brightness 65
6.2 Modelling the low-energy precipitation 67
6.3 Interpretation 78

7 Conclusions 84
7.1 Future work 85

Bibliography 88

List of Figures

1.1 The beautiful aurora 10
1.2 Auroral forms 14

2.1 Photograph of the SIF platform 18
2.2 Schematic of the HiTIES instrument 19
2.3 The three different HiTIES filter mosaics 20
2.4 An example TLC image 22
2.5 Photograph of the EISCAT Svalbard Radar 24

3.1 Initial intensity calibration of HiTIES data 28
3.2 An example keogram, for the period 15 UT - 21 UT on 26 January 2006 31
3.3 Calibration results for stars identified in 26 January 2006 data between 15 UT and 21 UT 32
3.4 Typical spectral flux from a G class star, according to Allen [1973] 34
3.5 Intensity calibration results 36

4.1 Locating the magnetic zenith in a camera image 39
4.2 Points tested within the model ionosphere when calculating the position of the magnetic zenith 42
4.3 Colour plot of points tested within the model ionosphere 43
4.4 Angular distance between the magnetic zenith as found using camera data and the pointing direction of the ESR in its "field-aligned" position. 45
4.5 Theoretical zenith points for different altitudes plotted within a TLC image, as used for transforming the coordinate system . 46
4.6 The motion of the auroral zenith over a period of 5 s at the start of the event studied 48

4.7 The motion of the auroral zenith over a period of almost 15 s at the end of the event studied 49
4.8 x′ and y′ for the entire rayed part of the event studied. 50

5.1 HiTIES and photometer data for the event studied 52
5.2 7320 Å O^+ emission line as measured by HiTIES, in a single 30 s exposure 53
5.3 Brightness of 7320 Å emission line from 17:26–17:30 UT 54
5.4 The ratio of intensities of the 7774 Å to 5149 Å SIF photometers 56
5.5 EISCAT Svalbard Radar (42 m dish) data for the event studied 59
5.6 High resolution ESR data for 17:27–17:30 UT 60
5.7 Zenith motion compared with photometer data 62

6.1 Electron transport and ion chemistry model flow diagram 64
6.2 HiTIES, ESR and photometer data for the period 17:26–17:30 UT 68
6.3 Model run with Maxwellian input spectra 70
6.4 Model run with Gaussian input spectra 71
6.5 Model run with Gaussian input spectra at reduced peak energies 72
6.6 Model run with combined Gaussian and Maxwellian spectra . . 73
6.7 Model run with very low energy precipitation 75
6.8 Model run with pulsed mono-energetic input spectra at 20 eV peak energy 76
6.9 Model run with pulsed mono-energetic input spectra at 50 eV peak energy 77
6.10 TLC images for the first part of the event 79
6.11 TLC images for the latter part of the event 80
6.12 Diagram showing the ESR beam during coronal aurora 82

List of Tables

1.1 Auroral emissions encountered in this study 13

6.1 Transitions making up the 7320/7330 Å doublet 66

Acknowledgements

Although the work here is my own, many people are owed thanks for the help given to me in the production of this thesis. Most of all I would like to thank my supervisor, Betty Lanchester, for all her encouragement and support both during this course and previously. Nickolay Ivchenko has also been of great assistance concerning calibration matters and the ion chemistry model, and I would also like to thank him for giving me the opportunity to spend time in Stockholm and letting me stay in his house. Jo Sullivan somehow managed to keep me (relatively) sane in Southampton and at stupid o'clock in the morning on Svalbard, and has always been there to help answer my questions, even when she was trying to relax at home. Hanna Dahlgren has been a wonderful friend both on campaign and elsewhere, and we have had many useful discussions on things as diverse as auroral emissions and toenails. Olli Jokiaho has single-handedly kept up my pub lunch quota, and has also helped me to understand several features of the auroral spectrum. Mina Ashrafi has helped with the ion chemistry model, and I also thank her for introducing me to delicious Iranian food. I would also like to thank Urban Brändström, Fred Sigernes and Björn Gustavsson for useful discussions regarding the definition of the unit Rayleigh and intensity calibration in general. Björn also deserves thanks for keeping me entertained in Tromsø and on Svalbard, and for trying to teach me to ski! I would also like to thank Helen Richmond for playing the "hunt-the-spelling-mistake" game on our long bus journey to York.

In addition to those named thanks are also due to the campaign team, auroral station managers and EISCAT staff who worked many anti-social hours to obtain the data I have used. Finally I acknowledge those who have provided financial support: The University of Southampton for my MPhil funding; PPARC for supporting SIF; the funding agencies of China, Finland, France, Germany, Japan, Norway, Sweden and the UK for supporting EISCAT.

A lullaby too rough: I never saw
The heavens so dim by day. A savage clamour!
Well may I get aboard! This is the chase:
I am gone for ever.

[Exit, pursued by a bear.]

The Winter's Tale
WILLIAM SHAKESPEARE

Chapter 1

Introduction

Figure 1.1: The beautiful aurora. Photograph taken by the author in Ramfjordmoen, near Tromsø, Norway, 18 October 2006.

The aurora is a very beautiful phenomenon, as testified by the photograph shown in figure 1.1. It has enthralled many generations of people from many different civilisations inhabiting the northern polar region, and also lower latitudes. It is often explained in folklore using poetic images, such as the Finnish *revontulet*; foxes made of fire sending sparks up into the sky as they run across

the snow. We now know more about the mechanisms leading to the aurora, and the study of it leads to advances in many areas of science and technology as diverse as oil exploration, global climate change and human spaceflight.

This work investigates rayed aurora within the magnetic zenith, and quantifies some short-term changes exhibited by it. These short-term changes are related to perturbations of the Earth's magnetic field, and could lead to the estimation of currents in the ionosphere. The work also demonstrates the importance of considering auroral structure when analysing measurements made by instruments which do not observe it directly, particularly those employing the incoherent scatter radar technique.

All data shown throughout this study was acquired on 26 January 2006, using a variety of instruments based on Spitsbergen, the largest island in the arctic archipelago of Svalbard. Svalbard's location in the high arctic (78° north, 16° east) make it ideal for studying both nightside and dayside aurora. The instruments used in this work include a high-resolution spectrograph, a video camera and photometers, together making up the Spectrographic Imaging Facility (SIF). Data from the EISCAT Svalbard Radar has also been used. All of these instruments are described in chapter 2. Chapter 3 explains a new method developed for the absolute intensity calibration of the SIF spectrograph using the stars observed by it during normal operation.

The main body of work done is demonstrated and discussed in chapters 4 and 6. The auroral event studied in this thesis occurred at approximately 17:25–17:30 UT on 26 January 2006. For relatively long periods of this event very clear coronal rays were observed. The position of the magnetic zenith has been found from the alignment of these rays, and short-term changes in this position have been quantified and interpreted in relation to the EISCAT radar. This work is shown in chapter 4. Data from SIF and EISCAT at the time of the event are shown in chapter 5, and some analysis techniques are explained. This data is interpreted further in chapter 6, where model results are also shown. Conclusions are drawn and recommendations for future work are given in chapter 7.

1.1 Theoretical background

This section summarises some of the theoretical background most relavent to the work presented in this thesis. For more detailed information see the many textbooks on the subject of space plasma physics and the aurora. Specific information is also explained in the appropriate chapters of this thesis.

1.1.1 The aurora

The aurora is a result of the Sun's interaction with the Earth. Electrons and protons form the solar wind flowing outwards from the Sun. These particles can be transferred from interplanetary space into the Earth's magnetosphere by magnetic reconnection. They then spiral around the Earth's magnetic field lines, funnelling into the ionosphere at the polar regions. Collisions between the solar wind particles and the ions, molecules and neutral atoms populating the ionosphere result in many different electronic transitions, causing the emission of photons at different wavelengths. These emitted photons are observed as the aurora. The most predominant auroral emission line at 557.7 nm is produced by atomic oxygen, although the auroral spectrum is rich with many other features. The diversity of this spectrum provides many opportunities for inferring information about the atmosphere, magnetosphere and Sun-Earth system.

Various auroral forms are observed, although the theories leading to the different forms, particularly small-scale structure, are not yet well defined. The aurora can be highly dynamic, with structures moving and changing on timescales well below 1 second. It can also be relatively quiet and diffuse, with little structure observed. The aurora can be studied on a very wide range of spatial scales, from large-scale systems extending over hundreds and even thousands of kilometers, to very small-scale structures on the sub-km scale. Various medium-scale forms are shown in figure 1.2 (taken from [Kivelson and Russell, 1995]). These can exhibit small-scale structures within them, but will most likely also be a part of a larger system themselves. The top and third pictures in the figure show diffuse forms of aurora (homogeneous arc and homogeneous band respectively), with few clear fine structures. The remaining pictures all show forms which contain rays, and are usually dynamic. Auroral rays highlight the Earth's magnetic field lines, and so can be used to study

Wavelength	Species	Altitude	Precipitation
7774 Å	O	F-region	Low-energy electrons
	O_2	E-region	High-energy electrons
7320 Å	O^+	F-region	Low-energy electrons
5149 Å	N_2^+	E-region	High-energy electrons
4880 Å	N_2	E-region	High-energy electrons
4861 Å	Hβ	E-region	Protons

Table 1.1: Auroral emissions encountered in this study.

the Earth's magnetic field. The majority of the work done as part of this study concentrates on coronal rays, as shown in the bottom-centre picture in figure 1.2.

1.1.2 The ionosphere

The ionosphere is a layer within the atmosphere characterised by the fact that partially ionized plasma is continually maintained, coexisting with the neutral species. This allows electric currents to flow within the ionosphere. The layer is in turn made up of three main regions: the D region below 90 km altitude; the E region between 90–130 km; and the F region above 130 km. These altitude ranges are not strictly defined. Among other differences the ion composition of the three regions varies. In the case of the D region negative ions are in majority, whereas in the E region positive molecular ions are most common (mainly O_2^+ and NO^+). In the F region there is a transition from molecular ions at the lower altitudes to positive atomic ions higher up (mainly O^+).

1.1.3 Auroral emissions used in this study

A summary of the auroral emissions used in this thesis is given in table 1.1. It lists the type of precipitation and the ionospheric species giving rise to each emission, together with the approximate emission altitude within the ionosphere. These emissions are explained in more detail in this section. Note that the unit used for wavelength throughout this thesis is the ångström (Å), which is equivalent to 0.1 nm.

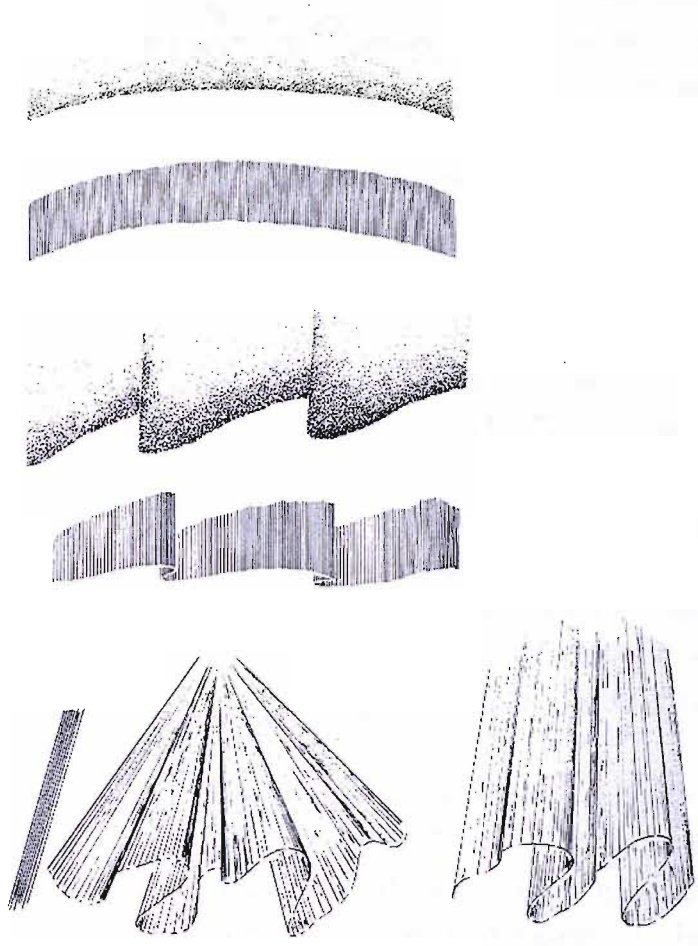

Figure 1.2: Various typical auroral forms, taken from [Kivelson and Russell, 1995]. From top to bottom: homogeneous arc; arc with rays; homogeneous band; band with rays. The bottom three forms are (from left to right): rays; corona; curtain.

7774 Å

Both O atoms in the F-region and O_2 molecules in the E-region are responsible for the auroral 7774 Å emission. The transition producing this emission is a decay from O(3p ^{5}P) to O(3s $^5S^0$). In the case of the O_2 molecules the emission is caused by dissociative excitation, whereby one or both of the resulting O atoms is in the 3p ^{5}P state. In the case of low-energy precipitation O atoms in the F-region are excited to the 3p ^{5}P state by direct electron impact. These O(3p ^{5}P) atoms then decay emitting at 7774 Å. The 7774 Å emission is useful in aurora studies due to the fact that it correlates with electron precipitation both at high and low energies. This is most advantageous when the 7774 Å line is studied with other emissions.

7320 Å

The auroral 7320 Å line arises from emission by O^+ ions. Atomic oxygen is ionized by low-energy electron precipitation (< 1 keV) to O^+ in the $^2P^o$ state. This state is metastable, with a lifetime of approximately 5 s. It decays to the $^2D^o$ state, emitting at wavelengths of 7320 Å and 7330 Å [Rees et al., 1982]. The 7320 Å emission is a result of the electric quadrupole and magnetic dipole transitions from the $^2P_{3/2}$ level to the $^2D_{5/2}$ level, and the magnetic dipole transition from the $^2P_{1/2}$ level to the $^2D_{5/2}$ level. The 7330 Å emission is a result of the electric quadrupole and magnetic dipole transitions from the $^2P_{1/2}$ and $^2P_{3/2}$ levels to the $^2D_{3/2}$ level [Ralchenko et al., 2008].

The relatively long lifetime of this emission should be considered when using it to study the aurora. Dahlgren et al. [2008a] have exploited this characteristic to study plasma flows in the ionosphere. However, the long lifetime could also prove problematic when studying aurora on short timescales. In the case of this study it has minimal effect, as the HiTIES spectrograph data used has a time resolution of 30 s, significantly longer than the emission lifetime.

5149 Å

The 5149 Å emission is a part of the N_2^+ first-negative system (it is the N_2^+1N (1,4) band) [Vallance Jones, 1974]. Emissions in the N_2^+1N system are a result of direct impact excitation by high-energy electrons on N_2.

4880 Å and 4861 Å

These two emissions are used for studying proton aurora. Both wavelengths contain the N_2 Vegard-Kaplan band, which is caused by electron impact on N_2 molecules in the E-region. However, the emission at 4861 Å is the Hβ line in the Balmer series, which is emitted as a result of proton precipitation. The line is doppler shifted to shorter wavelengths, as the emitting hydrogen atoms are mostly moving towards the observer on the ground. The 4880 Å measurement is used to subtract the effect of the N_2 Vegard-Kaplan band from the 4861 Å observation, allowing proton precipitation to be identified.

Chapter 2

Instrumentation

2.1 The Spectrographic Imaging Facility

The Spectrographic Imaging Facility (SIF) is a platform of instruments designed to allow various detailed studies of the aurora. It is a collaboration between the University of Southampton and University College London, and is located at the auroral station on the island of Spitsbergen, which is part of the Svalbard archipelago in the high arctic. Until November 2007 the facility was at a latitude of 78.20° north and a longitude of 15.83° east, allowing for measurements of the dayside aurora. During November 2007 the facility was moved approximately 7 km east to a new optical station, the Kjell Henriksen Observatory (KHO), in order to reduce the light pollution seen from the growing town of Longyearbyen. The new station (KHO) is at a latitude of 78.14° north and a longitude of 16.04° east. SIF includes a sophisticated spectrograph which permits measurements of several non-contiguous wavelength ranges at a high spectral resolution, which is explained further in section 2.1.1. It also has four photometers with a selection of interchangeable narrow passband spectral filters, and a white light auroral imaging camera equipped with a 645 nm high pass cut-off filter. The camera (The Little Camera, known as the TLC) has a field of view of 16.0°×12.8° to provide ideal support for the HiTIES spectrograph. All of the instruments which make up SIF are coaligned pointing at the theoretical magnetic zenith.

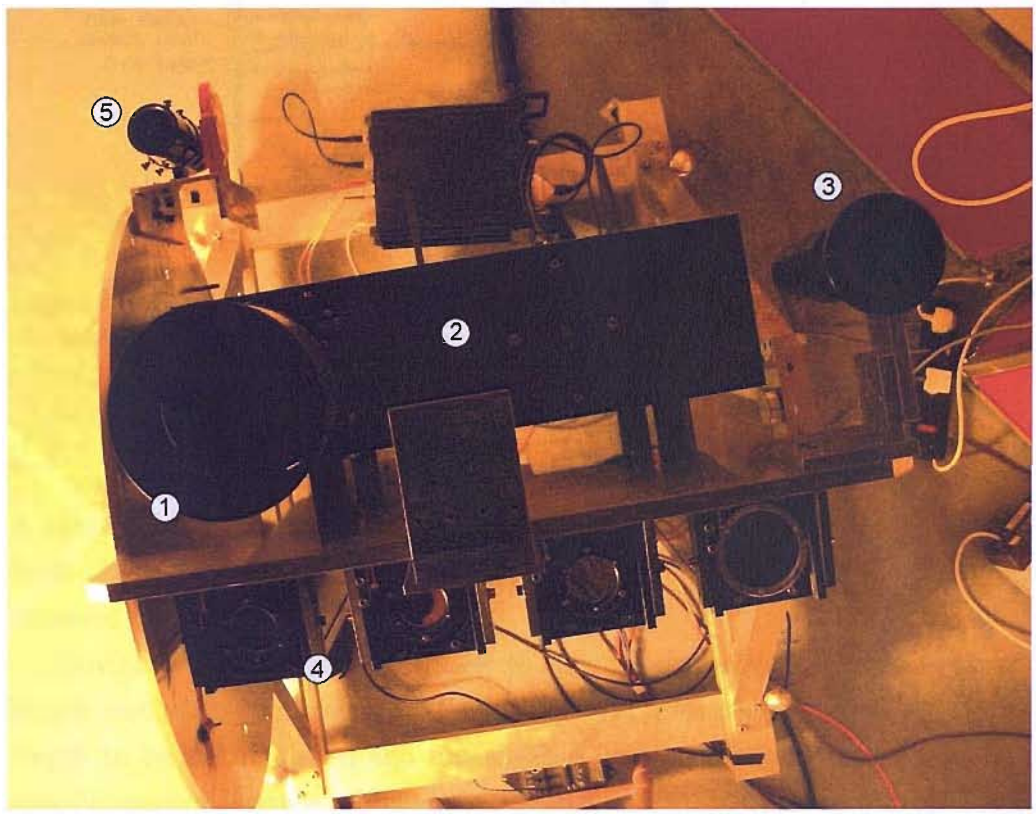

Figure 2.1: A photograph of the SIF platform taken from directly above it. The parts labelled are as follows: (1) The HiTIES field lens; (2) the HiTIES spectrograph body; (3) TLC imager; (4) photometers; (5) a sighting scope, to assist in aligning the platform.

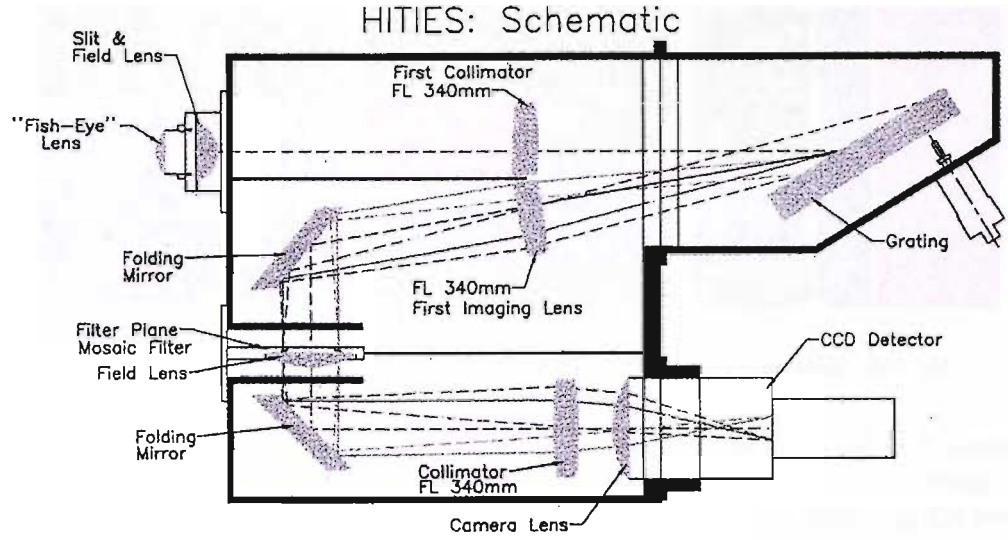

Figure 2.2: Schematic of the HiTIES instrument, from [Chakrabarti et al., 2001]. In the Southampton-UCL version of the spectrograph the fish-eye lens is replaced with a lens providing the slit with an 8° length.

2.1.1 HiTIES

A spectrograph facilitates measurements of the spectrum emitted by (or reflected by) a target. In this case the target is the ionosphere, and the emissions observed make up the aurora.

Obviously it is desirable to measure spectra at the highest possible wavelength resolution. This allows different spectral lines which are close in wavelength to be distinguished and investigated independently. When studying a specific spectral feature a higher wavelength resolution leads to a lower background level and more accurate intensity measurements of the feature in question. It can also be desirable to measure over a relatively large wavelength range, for example to observe different auroral emission lines simultaneously. With a conventional spectrograph a trade-off exists between the wavelength range measured and the resolution. More pixels (in the case of modern instruments) are needed to increase either property.

HiTIES overcomes this problem by using different parts of the CCD detector for different non-contiguous wavelength regions. Figure 2.2 shows the design of the instrument. Overlapping spectral orders from different wavelength ranges are focused and imaged simultaneously at the filter plane. Here the desired wavelength ranges are filtered separately by a mosaic of interfer-

(a) Mosaic filter #1 (b) Mosaic filter #2 (c) Mosaic filter #3

Figure 2.3: The three different HiTIES filter mosaics. The H-α and H-β panels are for the study of proton aurora. The various nitrogen panels allow the study of nitrogen rotational temperatures (see for example Jokiaho et al. [2008]) in electron aurora. Mosaic filter #2 (b) was designed primarily for supporting the Auroral Structure and Kinetics (ASK) instrument (see Ivchenko et al. [2008]). This was the mosaic in use during the event studied in this thesis.

ence filters. The CCD detector records an image of the mosaic filter. In one image dimension the light is split in wavelength (the dimension parallel to the grating axis). The other image dimension is the spatial dimension, parallel to the slit length. As of January 2008 three different filter mosaics are available for use with HiTIES. These are shown in figure 2.3. Mosaic #2 was first used in December 2003, while mosaic #3 was introduced in January 2007. During January 2006 (and hence the event studied here) the 4–panel mosaic filter was in place (figure 2.3(b)).

The CCD detector has also been changed and upgraded several times. Since November 2005 HiTIES has used an Andor electron-multiplying CCD (EMCCD). This allows low light measurements to be made with a very low noise level. As a result of this HiTIES is able to run at a high time resolution while maintaining a good signal to noise ratio. In combination with the 4–panel filter mosaic the Andor CCD provides data with a wavelength resolution of approximately 0.04 nm/pixel.

HiTIES is wavelength calibrated using hydroxyl airglow emission lines and the solar Fraunhofer spectrum. Both of these can be seen in data acquired during a normal run. The absolute intensity calibration of the spectrograph is described in chapter 3. The pointing direction and slit geometry are calibrated by matching the times and positions of stars passing through the slit with

theoretical values from a star catalogue.

For more detailed technical information about the HiTIES spectrograph see [Chakrabarti et al., 2001] and [McWhirter et al., 2003]. EMCCDs are explained on the website of Andor Technology PLC and in other literature produced by the company.

2.1.2 TLC

The Little Camera (TLC) consists of an intensified CCD (ICCD) camera connected to a professional quality DV (digital video) recorder. This records video in the standard 625/50 "PAL" format at 25 fps, with an image size of 720×576 pixels. The commercial lens used provides the camera with a field of view of 16.0°×12.8°, resulting in a spatial resolution of approximately 0.02 degrees/pixel. The TLC camera observes in white light, but has a 645 nm high pass cut-off filter. This filters out many long-lived emissions (such as the 557.7 nm oxygen line) which would otherwise blur the structures observed with the camera.

The DV recorder is in turn connected to an S-VHS recorder, which also records to tapes in PAL format, but is able to adjust the frame rate. Typically the S-VHS recorder has been set to record at 5 fps. The advantage of this is that the tape is able to store 5 times more data (in terms of time length), but at the sacrifice of time resolution. During most observation campaigns the TLC has continually recorded to S-VHS tapes (at 5 fps) with the tapes changed manually every 20 hours, while the higher quality DV tapes have only been used during radar runs and other particular times, recording at the full 25 fps. The DV tapes were manually changed every 3 hours when used. When running HiTIES remotely the TLC S-VHS tapes have sometimes been kindly changed by the auroral station managers. In November 2007 the system was upgraded so that no video tapes are needed - the digital output from the DV recorder is connected to a computer, and the data are stored directly to the computer hard drive.

Note that the timestamp shown in TLC images throughout this thesis is incorrect; it is about 1 minute prior to the actual time. During the end of January 2006 the instrument was under remote operation. As a consequence of this the clock providing timestamps could not be corrected for drift. Satellite passes in TLC data from this time were matched with those observed by

Figure 2.4: An example TLC image. This is a frame taken from data recorded to S-VHS tape.

another imager operating simultaneously (The University of Tromsø's ODIN imager), allowing the TLC acquisition time to be correctly determined.

Another consequence of remote operation is a reduction in time resolution of the TLC. In order to maximise the length of time between tape changes the frame rate was reduced to 2.78 fps with the S-VHS recorder.

The TLC data has not yet been intensity calibrated - it has only been used for studying the shapes and structures of aurora. However, it would be possible to intensity calibrate it by developing a similar method to the HiTIES star-based intensity calibration explained in chapter 3. The pointing direction and geometry of the image plane is calibrated by matching the positions of observed stars to those in a star catalogue. This calibration produces a set of 8 coefficients which allow the accurate conversion from pixel coordinates to azimuth and elevation, and vice versa.

2.1.3 Photometers

Initially SIF included two photometers recording at different wavelengths, but in November 2004 an additional two were added. Photometers simply count photons. They are not sufficiently sensitive to record each individual photon, but their count rate (noise corrected) is proportional to the photon flux. They are susceptible to a certain degree of thermal noise.

The SIF photometers have a set of interference filters at various wavelengths, any of which can be used on any of the photometers. For the past four years the most common filters used have been 486.1 nm, 488.0 nm, 514.9 nm and 777.4 nm. These were the filters in use during the event studied in this thesis. The filters at 486.1 nm and 488.0 nm are used for studying proton aurora. The emission line at 777.4 nm comes from excitation of atomic oxygen in the F-region and dissociative excitation of molecular oxygen in the E-region, and is an indication of both low and high energy electron precipitation [Dahlgren et al., 2007]. The 514.9 nm emission comes from N_2^+1N, and is an indication of high energy electron precipitation or resonant scattering.

The typical time resolution of the SIF photometers has been 5 Hz, although they were designed to run at up to 10 Hz. They each have a field of view of approximately 1 degree, and are coaligned with the theoretical magnetic zenith.

Figure 2.5: Photograph of the EISCAT Svalbard Radar, taken from further up the mountain of Breinosa on 6 September 2007. The 32 m dish is to the left of the photograph, and the 42 m dish is to the right.

2.2 EISCAT

The EISCAT Scientific Association runs an incoherent scatter radar facility close to Longyearbyen on Svalbard, known as the EISCAT Svalbard Radar (ESR). This consists of two cassegrain dish antennas, with diameters of 32 m and 42 m. The antennas are not able to transmit simultaneously. The 42 m dish is fixed in the field-aligned position, while the 32 m dish is fully steerable. The ESR is located at a geographic latitude of 78.15° north and a geographic longitude of 16.03° east. This is approximately 7 km from the position of SIF during the event studied in this thesis. The new auroral station (KHO) is considerably closer to the ESR.

Incoherent scatter radar is a technique in which the back-scattered spectrum from the radio-illuminated ionosphere is recorded and analysed to derive several plasma parameters, the most important of which in this thesis are the electron density and the electron and ion temperatures. The modulation scheme applied to the radio transmitters and receivers affects the height range over which measurements are made, as well as the height and time resolutions. The conditions in the ionosphere will also affect the degree of post-integration

required to produce a clear spectrum that can be correctly analysed, therefore affecting the height and time resolution of the analysed data.

For more information about the incoherent scatter radar technique and EISCAT see for example [Rishbeth, 1978] and references therein.

The analysed radar data used in this thesis has a time resolution of 6.4 s, and covers a height range of about 100–600 km. The height resolution varies from about 5 km in the E-region to about 30 km at the higher altitudes.

Chapter 3

Absolute Intensity Calibration of the HiTIES Spectrograph

3.1 Aim of intensity calibration

Absolute intensity calibration is the process of converting a measured number of counts recorded by the spectrograph to a meaningful unit, such as Rayleighs per ångström[1]. This is essential for combining data sets from different times, instruments, or locations, and allows the data to be interpreted correctly and compared to model results.

3.2 Initial intensity calibration

Prior to the absolute intensity calibration process the spectrograph raw CCD images are corrected to remove background noise.

During a normal data run a set of images is taken regularly with the camera's mechanical shutter closed, known as "dark" images. These show only the dark current within the CCD and electronics, as the CCD is completely hidden from light sources. Occasionally a particular dark image will contain a small area of very bright pixels, caused by a cosmic ray passing through the CCD at the time of acquisition, so these images are discarded. The remaining images in a given set are averaged together pixel-by-pixel, to produce an overall approximation for the dark current measured by the CCD at that time.

[1]The ångström (Å) is a unit used for wavelength throughout this thesis, and is equivalent to 0.1 nm.

For each data image the most recent dark image is subtracted from it.

In addition to the dark images a further noise correction is made. As the temperature surrounding the camera electronics fluctuates, the amount of thermal noise recorded by the camera fluctuates. This cannot be corrected for by the dark images, as they themselves are also subject to variations in the thermal noise level. Due to the design of the spectrograph, the edge of the CCD remains unlit even when the shutter is open - the image of the mosaic does not fill the entire CCD frame. This allows a narrow strip of pixels which are always unlit to be used to remove the effect of thermal noise. For every single image, including dark images, a mean value is calculated for the same strip of unlit pixels (shown in figure 3.1(b)). This value is then subtracted from each pixel in the image. This has the effect of normalising all images to the unlit strip, so the thermal noise variation effects are removed from the data.

One final correction is made to the spectrograph data before the absolute intensity calibration. Data images recorded by the spectrograph show a variation in intensity due to the optics used; the area in the centre of the image is much brighter than at the edge, and a fresnel pattern is also present. In order to correct for this exposures are taken of a flat-field lamp. This lamp emits at an approximately constant brightness in the wavelength range of the spectrograph mosaic filter, and therefore any variations in intensity across the image are due only to the spectrograph optics. "Flat" images are processed in a similar way to the "darks" - removing cosmic ray contaminated exposures and averaging a set together, pixel-by-pixel. They also have an appropriate dark image subtracted from them, and the thermal noise accounted for with the normalisation strip. Data images are then divided by the nearest flat image, thereby removing the unwanted intensity variations.

The entire calibration process described in this section can be summarised with the equation

$$data = \frac{raw - dark}{flat - dark} \tag{3.1}$$

where all raw, dark and flat images are normalised to the same unlit strip. Examples of calibrated data, raw data and a flat image are shown in figure 3.1.

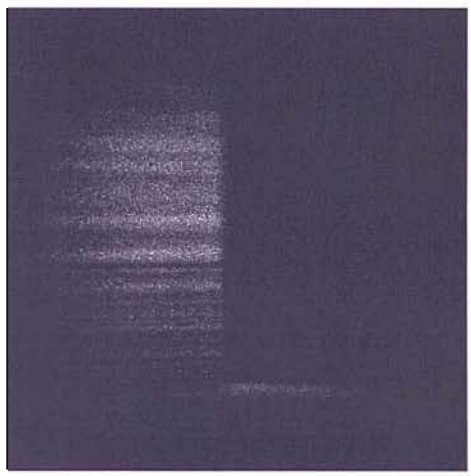

(a) Raw data image

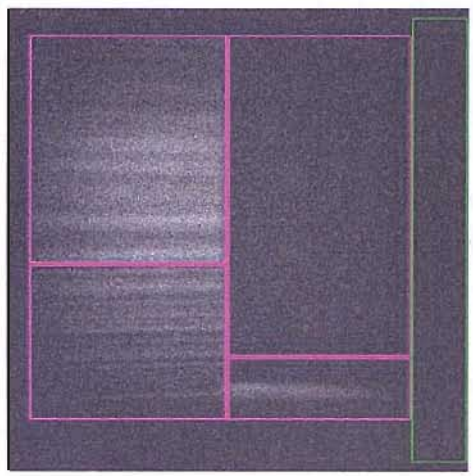

(b) Position of mosaic panels (pink) and unlit normalisation strip (green)

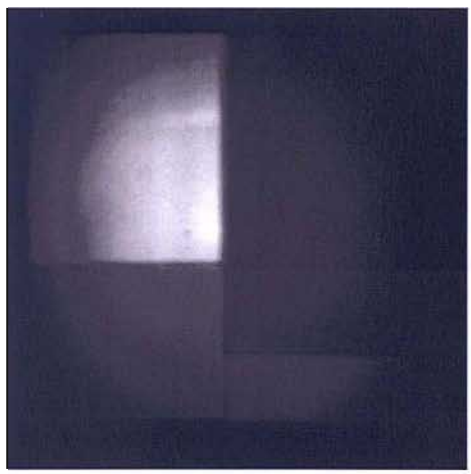

(c) Flat image

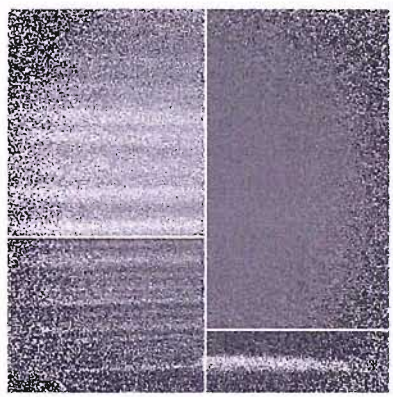

(d) Calibrated mosaic filter panels

Figure 3.1: Initial intensity calibration of HiTIES data. The calibrated data (d) shows more noise toward the edge of the image, as less light passes through the spectrograph. This is highlighted in the flat image (c).

3.3 Absolute intensity calibration using stars

By calibrating the SIF flat-field lamp used in the process described in section 3.2 measurements from the HiTIES spectrograph can be calibrated. This has been done twice during the instrument's lifetime using a method as demonstrated by Sigernes et al. [2007]. However, for periods where the flat lamp calibration is not available a method has been developed to calibrate the spectrograph using the stars which it records during a normal data run.

An absolute intensity calibration allows the brightness of an extended source such as aurora to be quantified in units of R/Å. Since stars are point sources, the equation for the received photon flux of a point source is compared to the equivalent equation for an extended source.

The number of photons received from a star in the spectrograph, in the average wavelength range of a single pixel, is

$$N_{phot,p} = F_\lambda \, \Delta\lambda \, A \, t_{star} \tag{3.2}$$

where $N_{phot,p}$ is the total number of photons received, $\Delta\lambda$ is the average wavelength range of a pixel in Å, F_λ is the flux of the star in photons $\mathrm{cm}^{-2}\,\mathrm{s}^{-1}\,\mathrm{Å}^{-1}$ in the range $\Delta\lambda$, A is the aperture area of the objective lens (i.e. slit area) in cm^2, and t_{star} is the time the star is visible in the slit in seconds.

The reason for taking the average wavelength range of a pixel rather than the total range of the filter panel will be explained below.

The time a star is visible in the spectrograph slit aperture can be given by,

$$t_{star} = \frac{W}{\omega_{star}} \tag{3.3}$$

where W is the slit width in radians and ω_{star} is the angular velocity of the star across the slit in $\mathrm{rad}\,\mathrm{s}^{-1}$.

The number of photons received can be related to the actual number of counts measured with an all-encompassing calibration constant,

$$N_{phot,p} \approx \alpha N_{count,p} \tag{3.4}$$

where the calibration constant α is made up of factors such as the detector efficiency and lens and dome transmission ratios. The approximate symbol is used because α may not necessarily be constant, but for this calibration to

work it is assumed to be constant over timescales of days. This should not be an unreasonable assumption to make.

Thus, combining equations 3.2, 3.3 and 3.4 we get

$$N_{count,p} = \frac{1}{\alpha} F_\lambda \, \Delta\lambda \, A \, W \, \frac{1}{\omega_{star}} \tag{3.5}$$

An equation similar to 3.2 can be given for an extended source. The rate of photons received in a single pixel, in photons s^{-1}, is given by

$$R_{phot,\Omega} = F_{\lambda\Omega} \, \Delta\lambda \, A \, \Delta\Omega \tag{3.6}$$

where $F_{\lambda\Omega}$ is the flux of an extended source in photons $cm^{-2}\, s^{-1}\, Å^{-1}\, srad^{-1}$, $\Delta\Omega$ is the acceptance solid angle of the pixel in question in srad, $\Delta\lambda$ is the wavelength range of the pixel in Å, and A is again the slit area, as in equation 3.2.

If we assume that all of the pixels in the panel have the same spectral width, then $\Delta\lambda$ in this case is equal to the average wavelength range of a pixel. Therefore $\Delta\lambda$ is identical in both equations 3.2 and 3.6.

$\Delta\Omega$ is simply the slit width, W, multiplied by the pixel length, l, both of which are in radians. Using this and factoring in the calibration constant α we obtain an equation for the count rate received from an extended source,

$$R_{count,\Omega} = \frac{1}{\alpha} F_{\lambda\Omega} \, \Delta\lambda \, A \, W \, l \tag{3.7}$$

Equation 3.5 can be rearranged to give,

$$\frac{1}{\alpha} \Delta\lambda \, A \, W = \frac{N_{count,p} \, \omega_{star}}{F_\lambda} \tag{3.8}$$

which can then be substituted into equation 3.7 to combine the fluxes from both point and extended sources into one equation,

$$R_{count,\Omega} = \frac{N_{count,p} \, \omega_{star}}{F_\lambda} \, l \, F_{\lambda\Omega} \tag{3.9}$$

This has the advantage of eliminating α, and with it all manner of things which would be difficult or tedious to include.

Equation 3.9 gives the count rate from an extended source, but this can be multiplied by the image exposure time, t_{exp}, to give the total number of counts

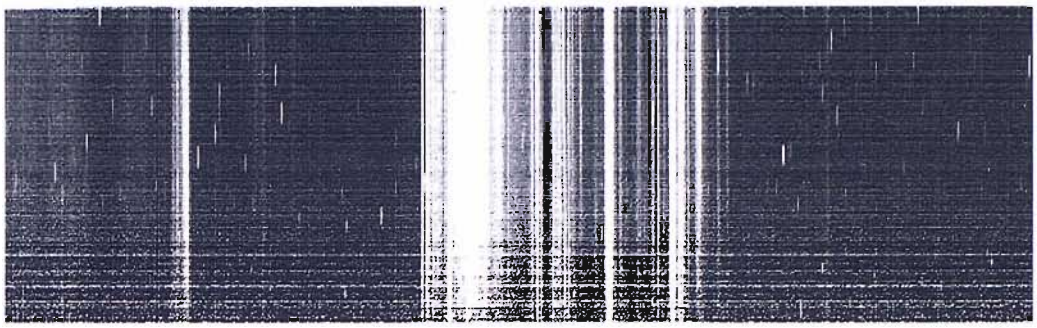

Figure 3.2: An example keogram, for the period 15 UT - 21 UT (l - r) on 26 January 2006. This shows data from the O^+ 7320/30 Å doublet mosaic panel. The bright areas mainly in the centre of the keogram are aurora, and the shorter bright vertical lines are stars.

measured in a pixel in one exposure.

$$N_{count,exp} = R_{count,\Omega}\, t_{exp} \tag{3.10}$$

Combining and rearranging equations 3.9 and 3.10 produces an equation for the flux received from an extended source, which gives the intensity axis for measured spectra.

$$F_{\lambda\Omega} = N_{count,exp} \frac{F_\lambda}{\omega_{star}\, l\, t_{exp}} \frac{1}{N_{count,p}} \tag{3.11}$$

The units of $F_{\lambda\Omega}$ are converted to R/Å by multiplying by $4\pi/10^6$ (for Rayleigh definition see [Hunten et al., 1956]).

To calibrate the spectrograph we first obtain a time series of slices of a clear period and identify a star present in it. This is known as a keogram, and an example is shown in figure 3.2. In this figure counts are averaged in the wavelength direction, in order to give $\Delta\lambda$ equal to the average range for one pixel (as used in equation 3.2). We then measure the total enhancement to the keogram caused by the star ($N_{count,p}$, total counts in the spatial and time dimensions, averaged in the spectral dimension), and calculate its theoretical spectral flux F_λ (see section 3.4) along with its angular velocity across the slit (ω_{star}). When calculating the theoretical spectral flux we assume a constant value across the wavelength range of the panel, and so taking an average value for $\Delta\lambda$ is justified. As we know the exposure time of the spectrograph images,

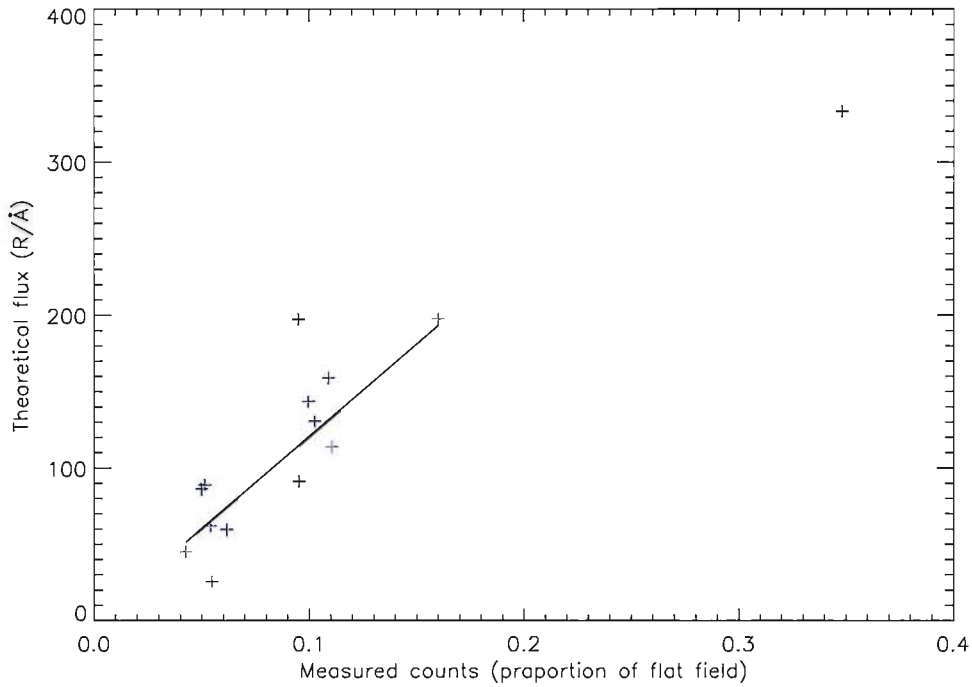

Figure 3.3: Calibration results for stars identified in 26 January 2006 data between 15 UT and 21 UT. Black crosses are considered outliers and are not included in the line of best fit calculation. This data has a correlation coefficient of 0.90.

we can then calculate the factor

$$\frac{F_\lambda}{\omega_{star}\, l\, t_{exp}} \frac{4\pi}{10^6}$$

for a large number of stars. This factor is plotted against $N_{count,p}$ (see figure 3.3), and a linear fit constrained to be through the origin is made. The perpendicular distances between the points and this initial fit are calculated, and those points further than 1 standard deviation from the line are discarded as outliers. The linear fit is then redone. The gradient n is the ratio of the flux of an extended source to the number of counts received in one exposure of the source.

$$F_{\lambda\Omega} = n\, N_{count,exp} \tag{3.12}$$

where $F_{\lambda\Omega}$ is now in R/Å. The value of n is then used as an absolute intensity calibration.

When using this calibration method it is important to consider what con-

stitutes a count. As the images used are normalised to a flat field image, what is actually compared is the ratio of the data image to the flat field image and the theoretical star flux, and so the resulting value n actually quantifies the flat field brightness. Therefore the calibration is only valid for data which are normalised with the same flat field. This also implies that when producing the calibration plot only star values which have used the same flat field image can be plotted together.

The star-based absolute intensity calibration method demonstrated here was used to calibrate the HiTIES data as used in chapter 5.

3.4 Calculating theoretical star fluxes

In order to calculate the theoretical flux of a star the star must be identified in a catalogue. Here the Smithsonian Astrophysical Observatory Star Catalog (SAO) was used. The star constellations in a data keogram can be matched to those in a computer generated theoretical keogram (created using the SAO and known geometry of the spectrograph slit), allowing the stars to be matched with their SAO numbers. The SAO catalogue gives the magnitude of the stars, along with their spectral types. These can then be used with data taken from [Allen, 1973] to produce a flux estimate in the range of the HiTIES filter panel. Allen gives the flux of a nominal zeroth magnitude star at 13 points in the range 1000 Å to 10000 Å for the seven spectral types. An example plot for G-class stars is shown in figure 3.4, with interpolation between the points. This can then be adjusted in intensity according to the magnitude of a particular star. The interpolated values in the range of the HiTIES filter panel are averaged to give a single flux value for each star in the keogram.

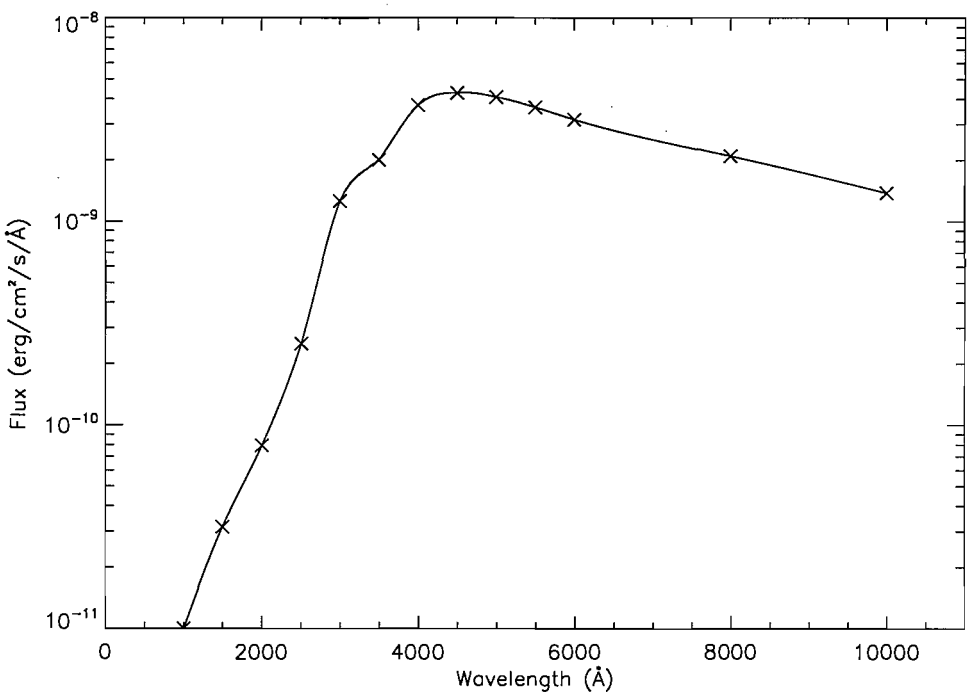

Figure 3.4: Typical spectral flux from a G class star, according to Allen [1973].

3.5 Comparison between star and lamp based calibration methods

The star-based calibration method has several advantages over calibrating the flat lamp directly. It can be implemented any time there is clear sky, and there is no need to transport the lamp to a special calibration lab. It also produces a calibration for ever single flat file. The lamp has been calibrated only twice in the past 10 years of operation, and so without the star method many flat files would be using a calibration which is years old.

However, the star method also has disadvantages. As the keograms used contain data which has been averaged in wavelength, it is not possible to obtain a wavelength-dependent intensity calibration. By calibrating the lamp directly a wavelength dependence can be determined.

There is also considerable scatter in the star calibration result plots (e.g. figure 3.3). This is due mainly to uncertainty in the theoretical star flux. Every star is assumed to have one of seven spectral shapes, but in reality there is more variation in star spectra. The HiTIES filter panels are also narrow in wavelength compared to the range given by Allen, so the values used are interpolated values. A potential improvement to the star-based calibration method would be to use a different star catalogue or spectra classification, which would result in more accurate star fluxes. Another source of scatter is the varying atmospheric conditions. Some stars may be observed through thin cloud, or indeed week aurora. Care is taken to only use stars during clear periods, but occasionally stars may be faintly obscured.

Figure 3.5 shows results from the two calibration methods. This shows they are in good agreement, and validates the star-based calibration.

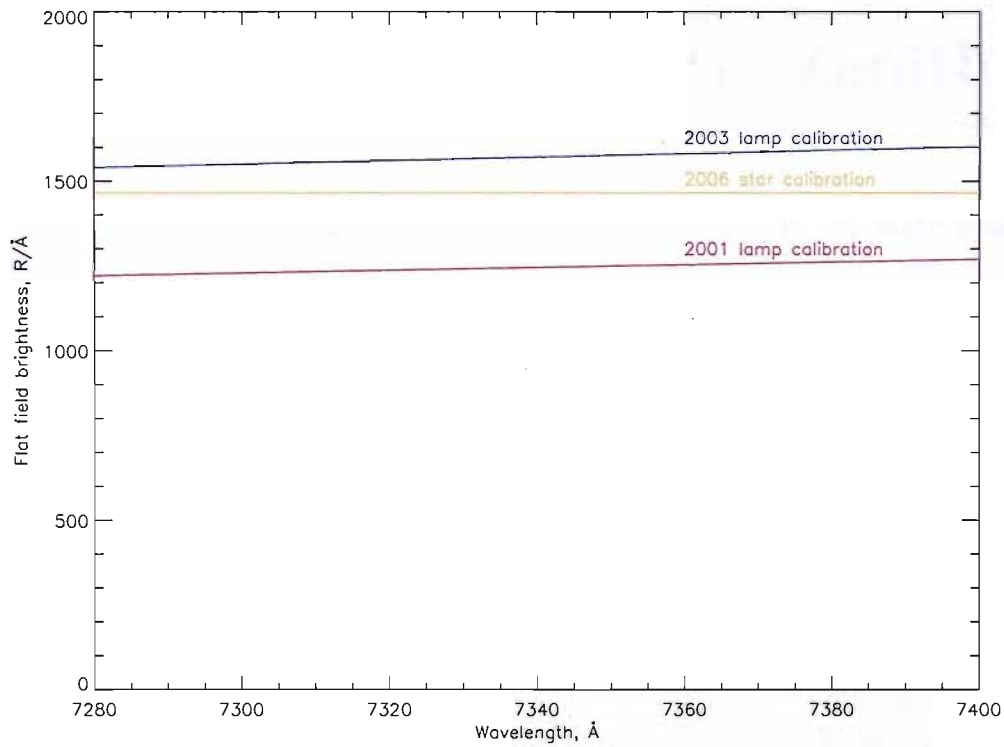

Figure 3.5: Calibration results from the 2 previous lamp calibrations, and the star-based calibration for January 2006.

Chapter 4

Short Term Changes in the Position of the Magnetic Zenith

This chapter is a continuation of work done by myself and Kirsty Walters as part of our undergraduate degrees.

4.1 What is the magnetic zenith?

The magnetic zenith is the position in the sky at which the Earth's magnetic field is pointing straight towards the observer (in the northern hemisphere). Auroral rays highlight magnetic field lines. As the observer looks directly at the magnetic zenith, all auroral rays will appear to converge at the zenith point, assuming all rays have the same height range. The zenith will be in a different place for different heights, due to the curvature of the magnetic field lines. It is simply the point where the look-direction of the observer is at a tangent to the field line.

The assumption is usually made that the magnetic zenith is at a constant location above an observer. This study challenges that assumption, and aims to determine the motion of the magnetic zenith during a particular event. There appears to be little similar work done previously. Velichko et al. [1985] investigated changes in the orientation of rays within auroral corona, and found many rays change orientation by a significant amount (of the order 1 - 10°). However, they do not appear to have studied motions of the magnetic zenith, only orientation changes of individual coronal rays.

4.2 Locating the magnetic zenith in camera data

The idea behind locating the auroral zenith is to trace the observed auroral rays so that the common intersection point of all the rays in an image can be found. In this study the rays are identified manually, within a computer program. For each ray several points are marked along it, and a straight line is fitted through the points by the program. Once all visible rays are identified in this way, the computer calculates the intersection point for every possible pair of rays. An average of these intersection points is then calculated to give the position of the auroral zenith. The average is calculated by expressing the intersection points as number of pixels in the x and y direction from the bottom left of the image, and then taking a median average in the x and y dimensions independently. Continuing to express all points in the image using the Cartesian pixel coordinate system described, further analysis is done to obtain a more accurate position for the zenith. The deviation of each of the possible intersection points from the median centre is found. The standard deviation of these values is then calculated, separately for the x and y direction. Any points outside of these standard deviations are then discarded as outliers, and a new median average and standard deviations are calculated. This central median point is used as the final auroral zenith location, with the standard deviations providing error estimates for the x and y coordinates. This process is demonstrated in figure 4.1.

By far the most common cause of outlying intersection points appears to be when two traced rays are found to be almost parallel. The resulting intersection point is then far away from the centre of the image, often outside the image frame itself. Rays can be near-parallel to each other when they are close together, or when they are on opposite sides of the zenith pointing at each other. It is not valid to calculate the zenith position based on the intersection of two such rays, as small changes to the clock angle of either ray as measured in the image will cause a large change in the intersection location. The human error associated with identifying the rays is not sufficiently small to allow these intersection points to affect the final result, hence they are discarded.

As the process of identifying the auroral zenith as described above involves a significant human component, the results will be slightly different each time

(a) Example image from the TLC

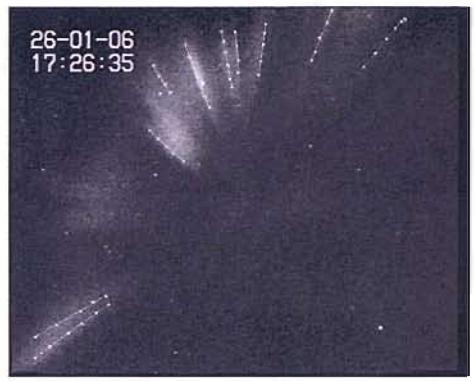

(b) Rays identified

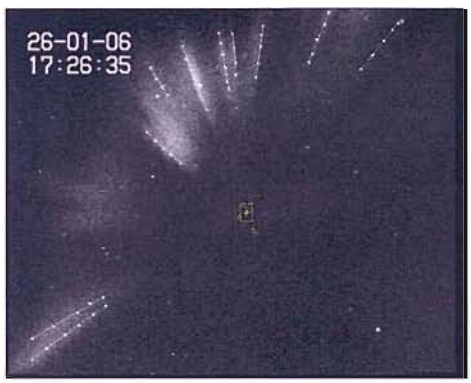

(c) Zenith position calculated from identified rays

(d) Zenith result improved with repetition of the process

Figure 4.1: Locating the magnetic zenith in a camera image. Firstly rays are identified manually (b). The computer then calculates the intersection points between each possible pair of rays. These are shown as yellow diamonds in (c). These are averaged to produce an estimate for the magnetic zenith position, along with an associated error (white diamond and box in (c)). This process is repeated, and the results combined to produce a more accurate zenith position (d). Note that the timestamp in this image is incorrect (see section 2.1.2). The actual acquisition time was 17:27:37 UT.

for the same data. This would be a disadvantage if the process was only carried out once. However, by repeating the process several times, the results can be combined to produce a result with a smaller error. This is more accurate than using a computer image analysis algorithm, which would produce the same result every time with the same error. In this study the same analysis has been carried out on the same data 5 times. A mean average of the 5 results was then calculated, weighted by the size of the error on each result. To get an overall error the standard deviation of the mean has been calculated.

4.3 Finding the magnetic zenith from a field model

The position of the magnetic zenith can also be calculated from a model of the Earth's magnetic field. This will obviously not take into account variations on short timescales, caused by specific solar or geomagnetic events, so will give a theoretical average position for the zenith. However, the method described in section 4.2 allows the actual short term changes of the zenith position to be obtained. By comparing the model zenith position to the actual zenith position information can be gained about the instantaneous geomagnetic conditions.

The magnetic model used in this study is the International Geomagnetic Reference Field, generation 10 (IGRF-10). This is produced by the International Association of Geomagnetism and Aeronomy (IAGA), and considers data from many satellites and observatories around the world. The model facilitates calculation of the geomagnetic field vector, and its rate of change, for any given location up to 600 km above the Earth's surface.

In order to calculate the position of the magnetic zenith from the IGRF model an iterative process has been developed. As explained previously the zenith is in a different position at different altitudes, and so the inputs to this process are the position of the observer (latitude, longitude, height above sea level) and the desired zenith altitude. A circular grid is arranged at the zenith altitude, centred on the observer, extending to a maximum of 20 degrees from the observer in geocentric coordinates. This grid consists of 5 rings with multiples of 6 points per ring (6 points for innermost ring, 30 points for outer ring). The magnetic field declination and inclination is calculated from the model at each of these points. These parameters are then used to find the

angle between the magnetic field at the point and the line-of-sight from the observer to the point. The magnetic zenith is where this angle is zero, and the observer is looking directly parallel to the field line. The grid point where this angle is a minimum is selected and used as the centre of a new grid when this process is repeated. At each iteration the total grid size is halved (i.e. in the second iteration the grid extends 10 degrees in each direction). The process is repeated many times, each time getting closer and closer to the magnetic zenith. For the analysis results shown in section 4.4 25 iterations were performed, giving an accuracy of the order 10^{-8} degrees in zenith position in geocentric coordinates, corresponding to a maximum error of less than 10^{-6} degrees in elevation. At this level the theoretical zenith position can easily be found to an accuracy of less than one pixel in the image frames. This can then be compared to the zenith as found in the auroral ray analysis.

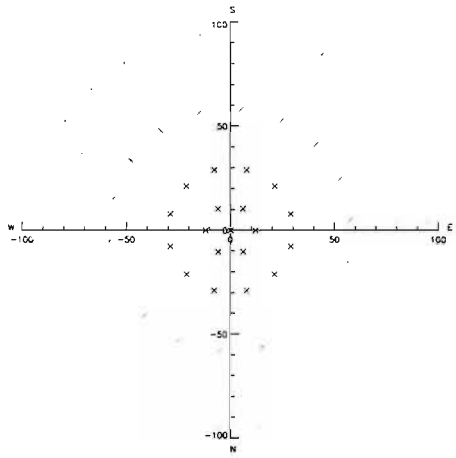

(a) Points tested in the first iteration only

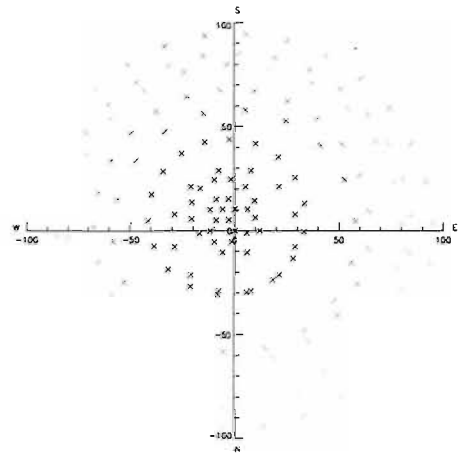

(b) First and second iterations

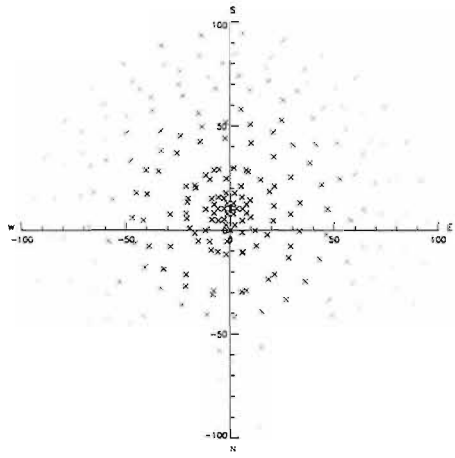

(c) First 3 iterations

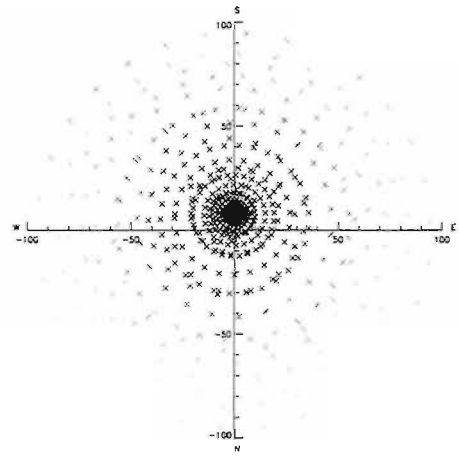

(d) All 25 iterations

Figure 4.2: These are the points tested within the model ionosphere when calculating the position of the magnetic zenith, for an observer located at SIF on 26 January 2006 and a zenith altitude of 200 km. This shows the points as viewed by the observer in degrees of elevation (zero straight up). The darker the cross the smaller the angle between the magnetic field line and the look direction of the observer. It is clear that many more points are tested close to the magnetic zenith. This is due to the iterative nature of the process.

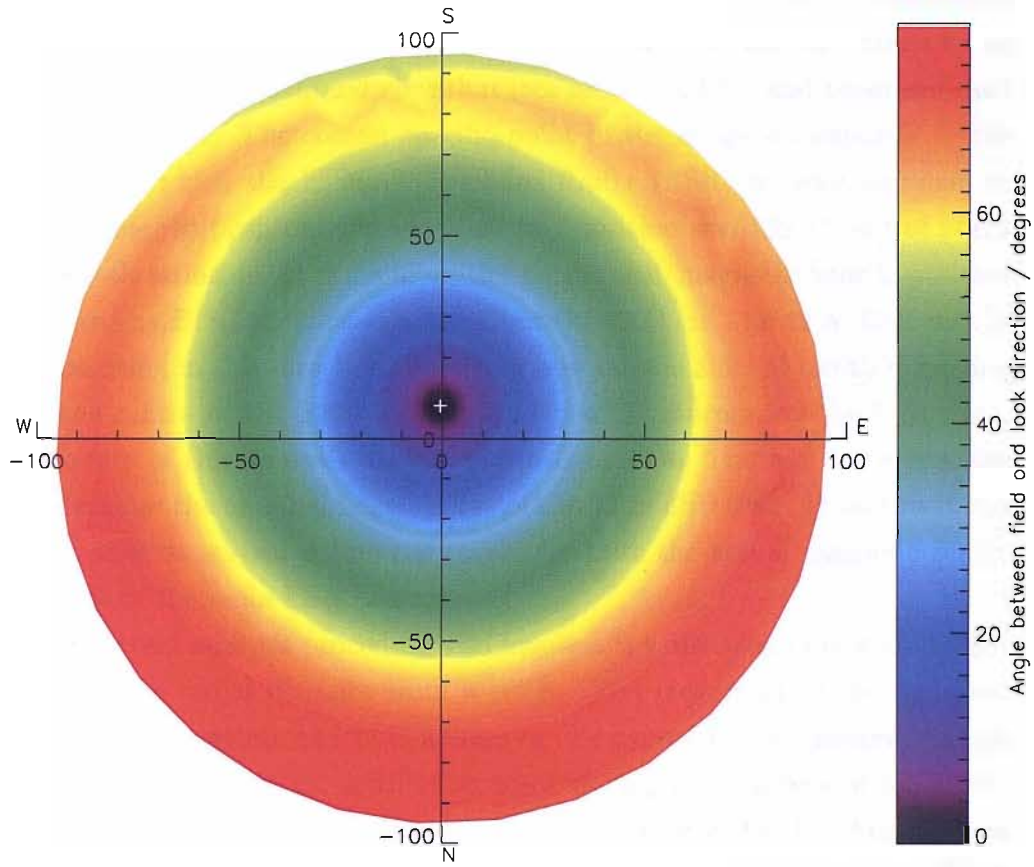

Figure 4.3: This shows the same data as in figure 4.2(d), but contours have been fitted around the points and shaded according to the colour scale shown. The white cross is the result - the calculated position of the magnetic zenith.

4.4 Analysis and results

The process described in section 4.2 was carried out for data from an event on 26 January 2006 between approximately 17:26 UT and 17:28 UT. This data set exhibits many auroral rays and coronal forms. The results have been analysed in two different ways.

Firstly the radial distance between a specific point in the image plane and the auroral zenith has been calculated, in degrees. A set of conversion coefficients are known which allow pixel coordinates within the image to be converted to an azimuth and elevation (see section 2.1.2), and these are used in this procedure. The chosen specific point in the image corresponds to the direction in which the EISCAT Svalbard Radar (ESR) is pointing when in the field-aligned position. During 2006 this position was 182.1° east of north with an elevation of 81.6°, and is the theoretical magnetic zenith position calculated by EISCAT for a zenith altitude of 300 km. The 42 m ESR dish is fixed pointing in this direction. Knowing how far the auroral zenith is moving from the centre of the ESR beam will help with interpreting the ESR data. The results of this analysis are plotted in figure 4.4. The red line across the plot identifies the nominal beam radius of the 42 m ESR dish. From this it can be seen that at several points the results indicate the actual magnetic zenith is outside of the main ESR beam.

The second analysis procedure also involves the direction of motion, rather than just the radial distance from a point. The movement of the apparent magnetic zenith within the TLC images can be caused by two different things; firstly that the magnetic zenith is actually moving in latitude and longitude, and secondly that the observed emissions are varying in height. Auroral rays could be observed and the zenith position calculated by tracing the rays. Then at an arbitrarily later time the emission from auroral rays could come from a different altitude. The magnetic zenith as found at this later time could appear to be in a different location, despite the field lines having not moved at all, due to the zenith being found for a different altitude.

Using the IGRF model the theoretical magnetic zenith position can be calculated for several different heights of auroral emission, as demonstrated in section 4.3. The twist of the Earth's field is sufficiently low that these points will lie in an approximately straight line when plotted in the camera image frame (see figure 4.5). A new coordinate system (x′, y′) is defined such that

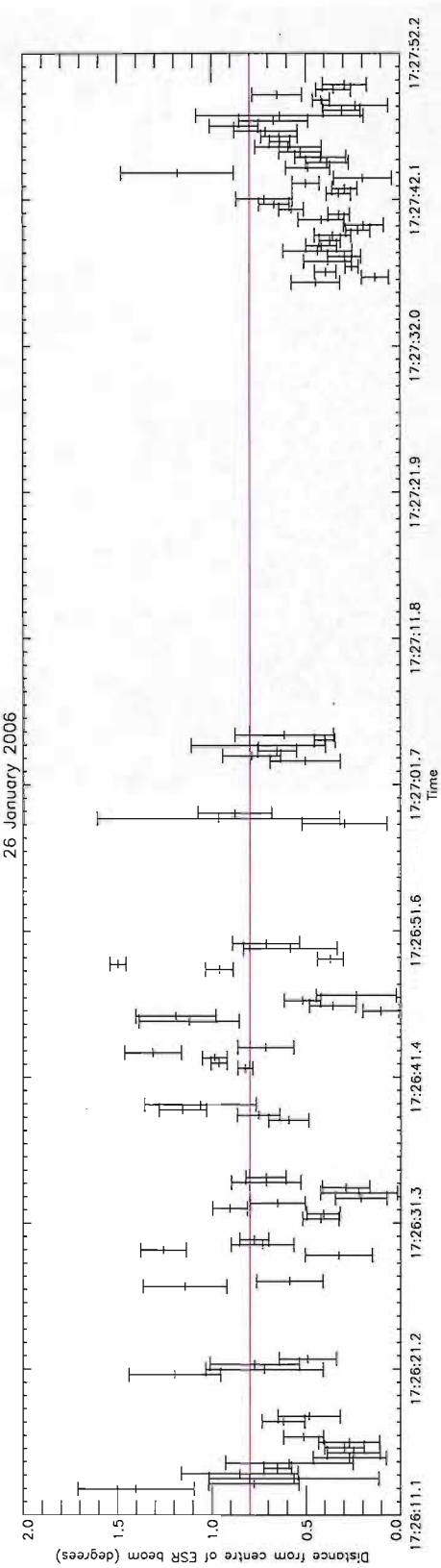

Figure 4.4: Angular distance between the magnetic zenith as found using camera data and the pointing direction of the ESR in its "field-aligned" position. The red line shows the edge of the nominal beam width of the 42 m antenna. The gap for most of the first half of the minute beginning 17:27 is due to a lack of aurora.

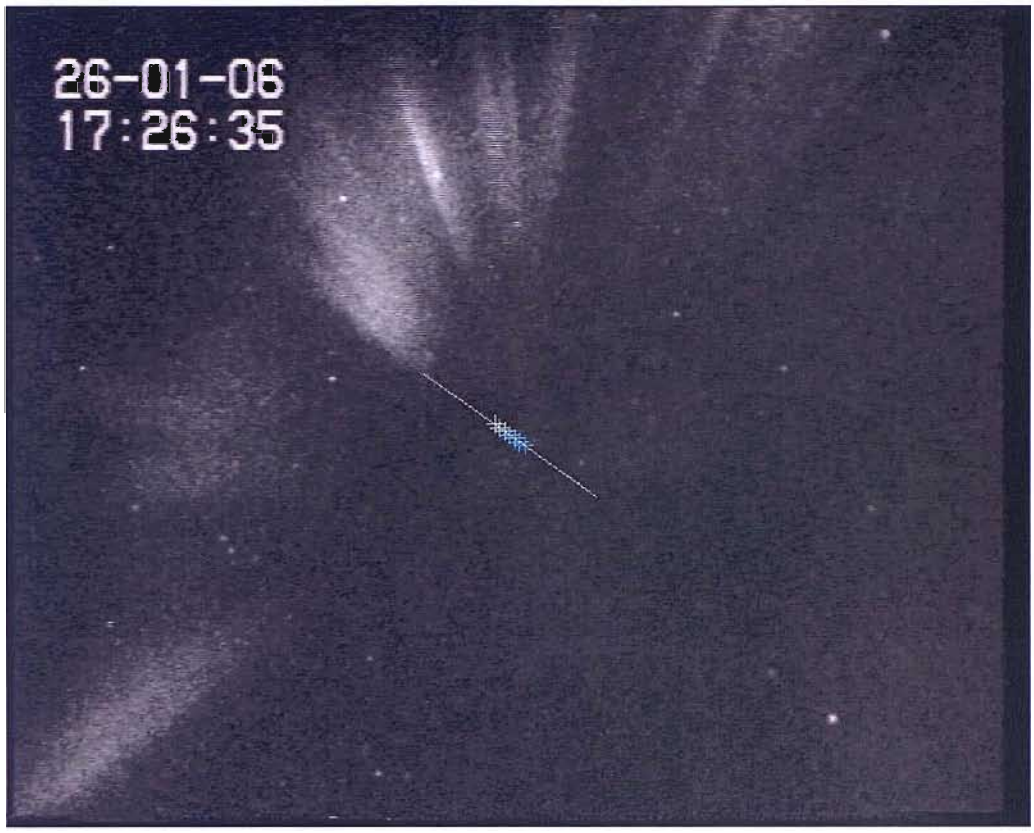

Figure 4.5: The theoretical zenith has been calculated from the IGRF model for altitudes between 100 km and 400 km, and is plotted in this image. A straight line has been fitted through these points. The top-most point (white) is for 100 km, and the bottom-most point (blue) is for 400 km. The zenith locations found by ray identification are transformed to a coordinate system using the fitted line shown here as the y′ axis direction, with the x′ axis perpendicular to this. The axes intersect at the model zenith point for 200 km altitude.

the y′ axis is parallel to a straight line fitted through the theoretical magnetic zenith calculated for 50 km altitude intervals between 100 km and 400 km, with the x′ axis perpendicular to this. The origin is defined as the 200 km altitude zenith calculated from the IGRF model. The zenith positions as found using the auroral method explained in section 4.2 have been transformed to this coordinate system. This allows zenith motions which could be caused only by emission altitude variation to be separated from actual changes in the Earth's magnetic field. Figures 4.6 and 4.7 show the x′ coordinate for the auroral zenith throughout the event studied. The dimension has been converted to degrees. Changes in this direction cannot be caused by auroral emission height variation. Figure 4.8 shows variations in x′ and y′ for the entire

rayed portion of the event studied. After the first few seconds y′ tends to stay more constant than x′, suggesting that the emissions are generally coming from the same height range. It is important to note that y′ cannot be tied directly to emission altitude, as the zenith could be moving in this direction due to actual changes in the Earth's magnetic field. A positive value for y′ could be an indication of aurora at low altitude, and a negative value could indicate aurora at high altitude. The zero point is for aurora at 200 km. There are several times when the zenith position in the x′ direction moves a substantial amount over short periods of time.

As there were two other cameras operating on Svalbard on 26 January 2006 roughly 7 km from the SIF TLC imager, the opportunity to triangulate the position of the magnetic zenith was considered. However, the zenith is a property of the location at which the camera is operating, and is not a single point within the ionosphere. It can be possible to triangulate the position of specific auroral features, such as a distinctive curl, providing they can be identified in both cameras. Unfortunately this can be more difficult to apply to rays due to the fact that there are usually many similar rays at different angles surrounding the zenith. It was decided that for this study it was not worth expending much effort on this time consuming process. Parallax measurements have been made by Ivchenko et al. [2005], successfully determining the altitude extent of auroral rays. The application of this method to the event studied here is recommended as a future continuation of this work.

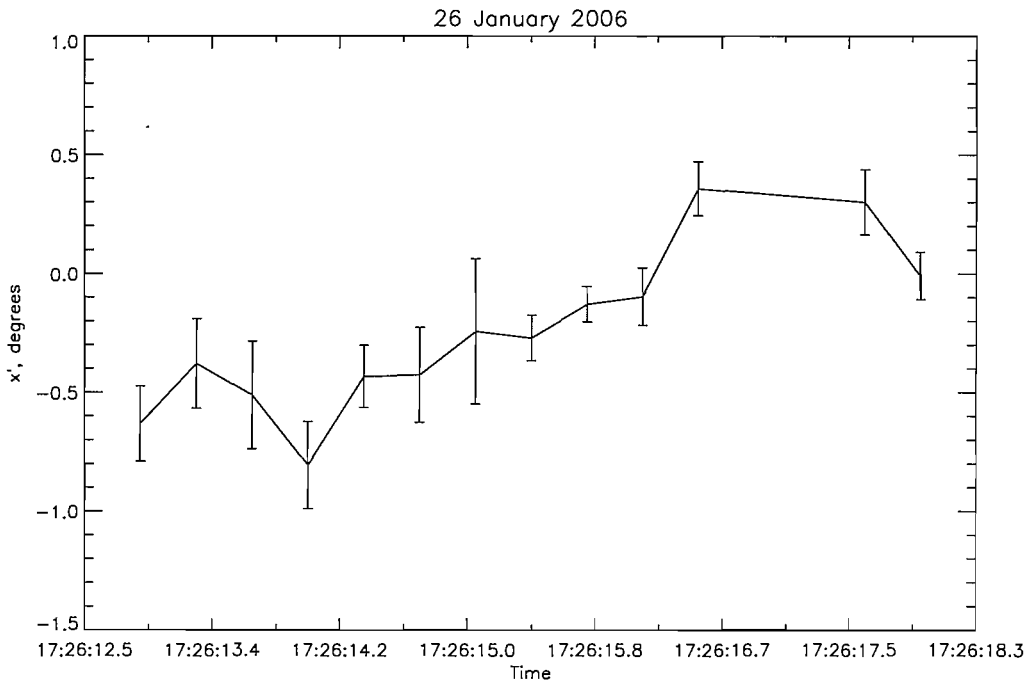

Figure 4.6: This shows the motion of the auroral zenith over a period of 5 s at the start of the event studied, in the x′ direction. Motions in this direction cannot be caused by changes in emission height.

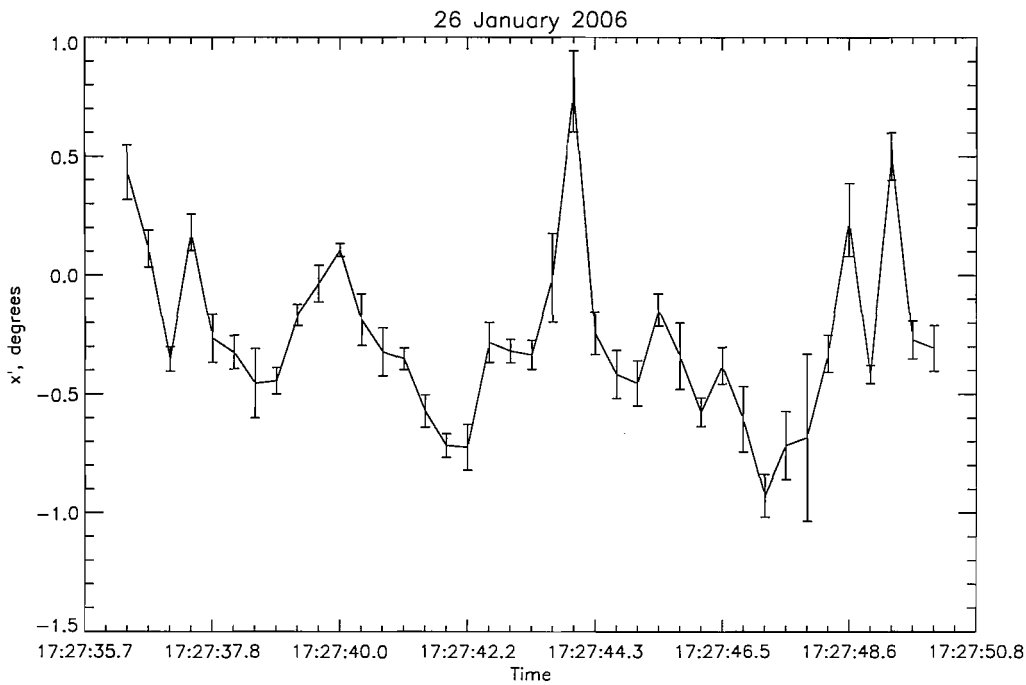

Figure 4.7: This shows the motion of the auroral zenith over a period of almost 15 s at the end of the event studied, in the x′ direction. Shortly after this the aurora began to display other more complex forms of an increased intensity, resulting in fewer well-defined rays.

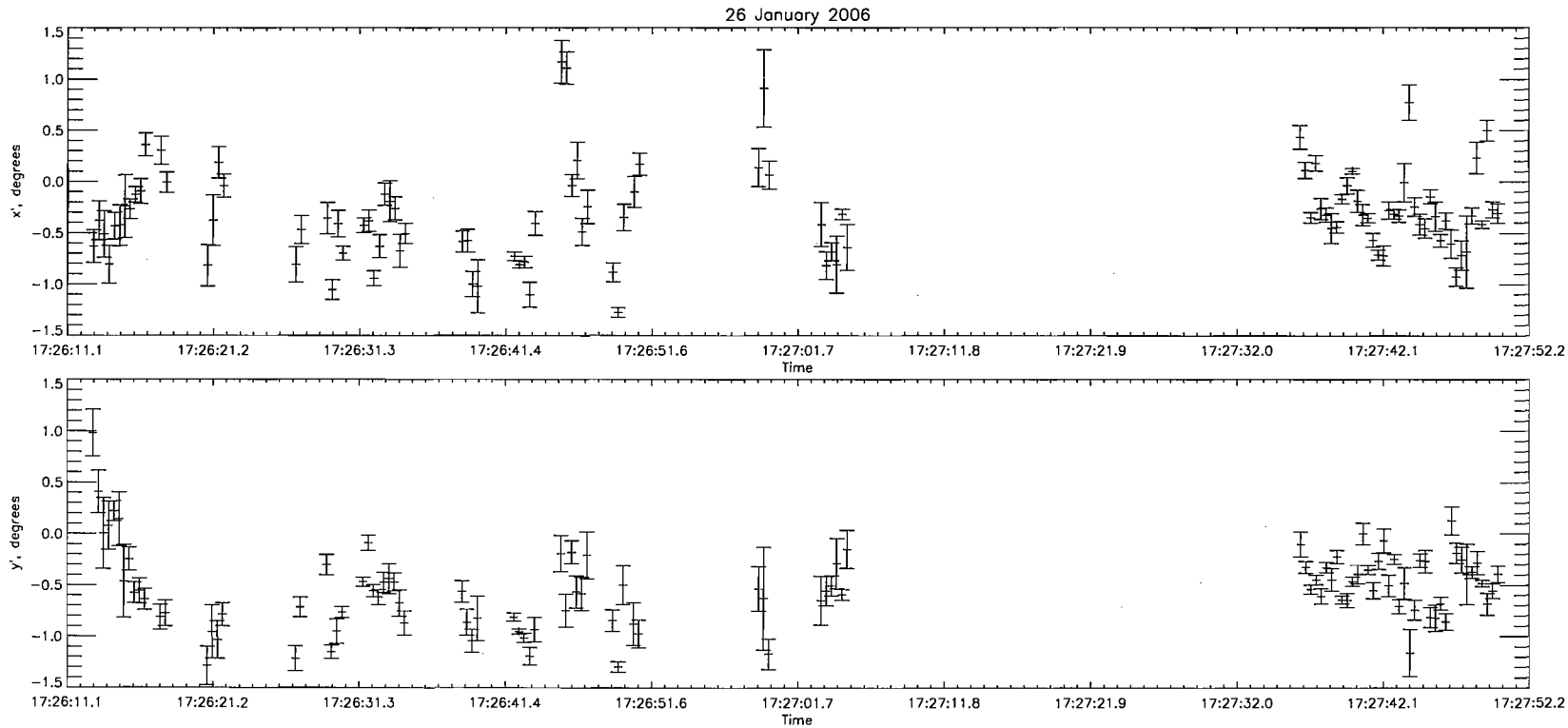

Figure 4.8: Both x′ (perpendicular to height variations) and y′ (parallel to height variations) for the entire rayed part of the particular event studied. The gap for most of the first half of the minute beginning 17:27 is due to a lack of aurora. Other small gaps are due to too little clear rayed structure being observed at that time.

Chapter 5

Spectrograph, Photometer and EISCAT Data

This chapter shows and discusses data from SIF and the EISCAT Svalbard Radar at the time of the rays analysed in chapter 4.

5.1 HiTIES data

Figure 5.1 displays data from HiTIES and the SIF photometers. The top four panels show data from the four different parts of the HiTIES filter mosaic, as shown in figure 2.3(b). This data has been calibrated using the star-based method explained in chapter 3. The HiTIES exposure time was 30 s, and the photometers were running at 5 Hz.

The O^+ spectrograph panel (top) shows hydroxyl airglow lines throughout the whole interval, for example at 7341 Å. However, the oxygen doublet at 7320 Å and 7330 Å is only visible when there is aurora, and is particularly strong between 17:26 UT and 17:27 UT, and also around 17:28 UT. It is clear that the aurora at 17:28 UT is of a different form, as there is also increased enhancement in the other panels, and in other parts of the "O^+" panel (from the N_2 1PG band; see [Dahlgren et al., 2008b] for discussion of the emissions in this wavelength region). The fact that the 7320/30 Å emission is so strong at 17:26–17:27 UT when compared to other simultaneous emissions suggests the event is caused by low energy electron precipitation only, whereas the aurora 1 minute later is caused by precipitation at a range of energies, both low and high.

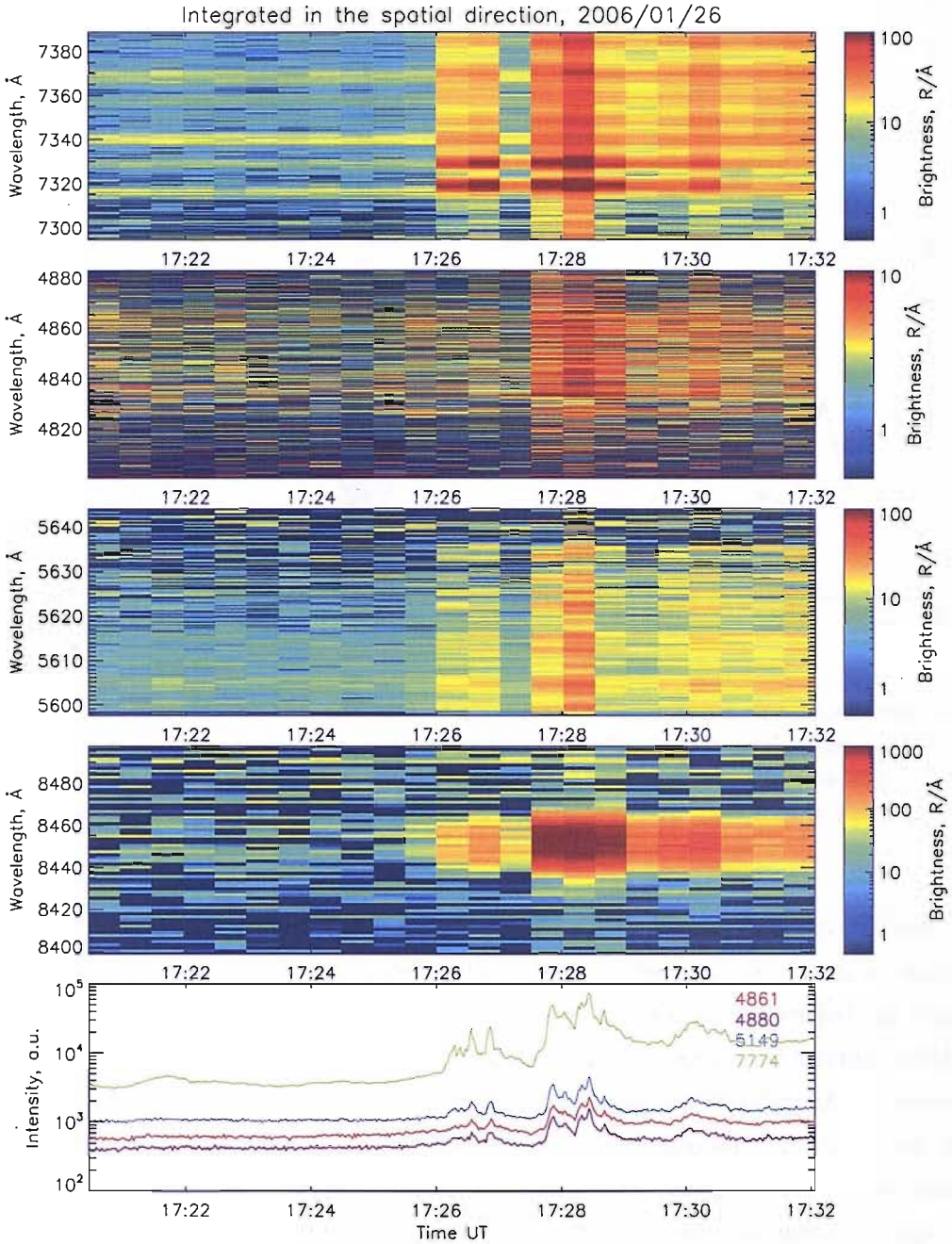

Figure 5.1: HiTIES and photometer data for the event studied. The top four panels show data from the four different panels of the HiTIES mosaic filter, and the bottom panel shows data from the photometers. The enhanced 7320 Å O^+ emission can be clearly seen in the top panel.

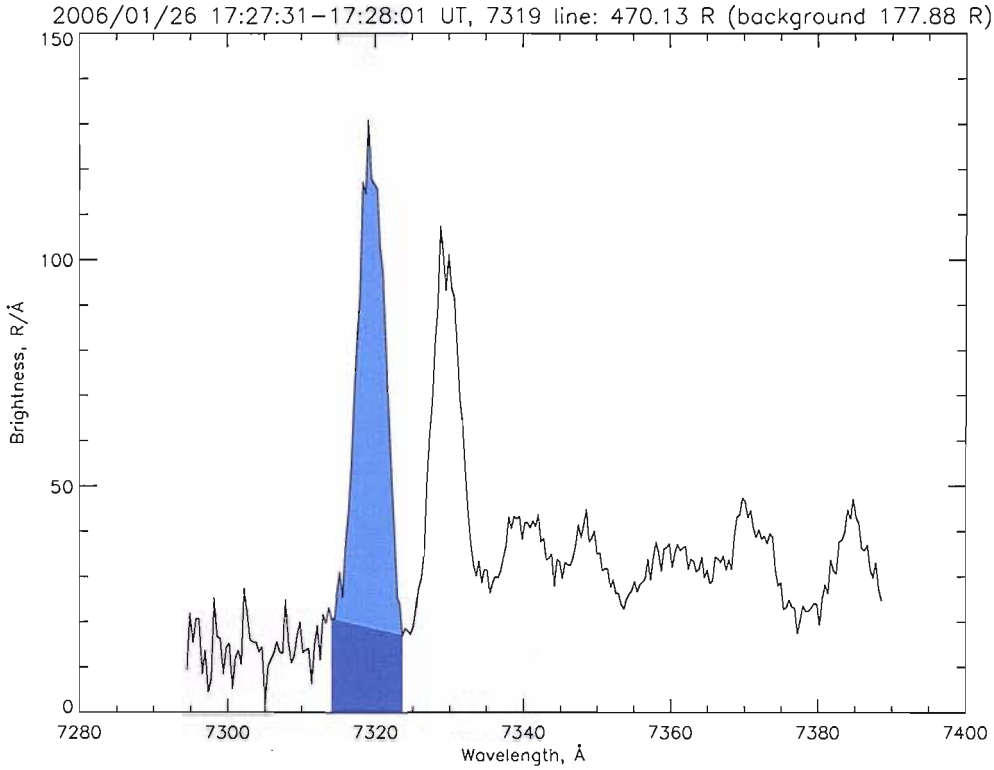

Figure 5.2: This shows the intensity of the 7320 O^+ emission line as measured by the HiTIES spectrograph, in a single 30 s exposure. The light blue shading indicates the area integrated to obtain a value for the total brightness of the emission. The total area under the curve is integrated, and then the dark blue area is subtracted as a background estimate.

The brightness of the 7320 Å O^+ emission has been calculated. Firstly the spectrograph data is averaged in the spatial direction, to obtain a single spectra. Only data from close to the centre of the slit are averaged, as this is where the signal to noise ratio is highest. The resulting spectrum (with brightness in units of R/Å) is integrated with respect to wavelength (in units of Å) in the pixel region over which the emission line is spread. This integration results in a single brightness value, in Rayleighs. A background level is then estimated by a straight line between the extremities of the affected region of the spectrum, and the area under this level calculated to obtain a single background value, also in Rayleighs. This is demonstrated in figure 5.2. The process was carried out for data from 17:26–17:30 UT, the results of which are shown in figure 5.3.

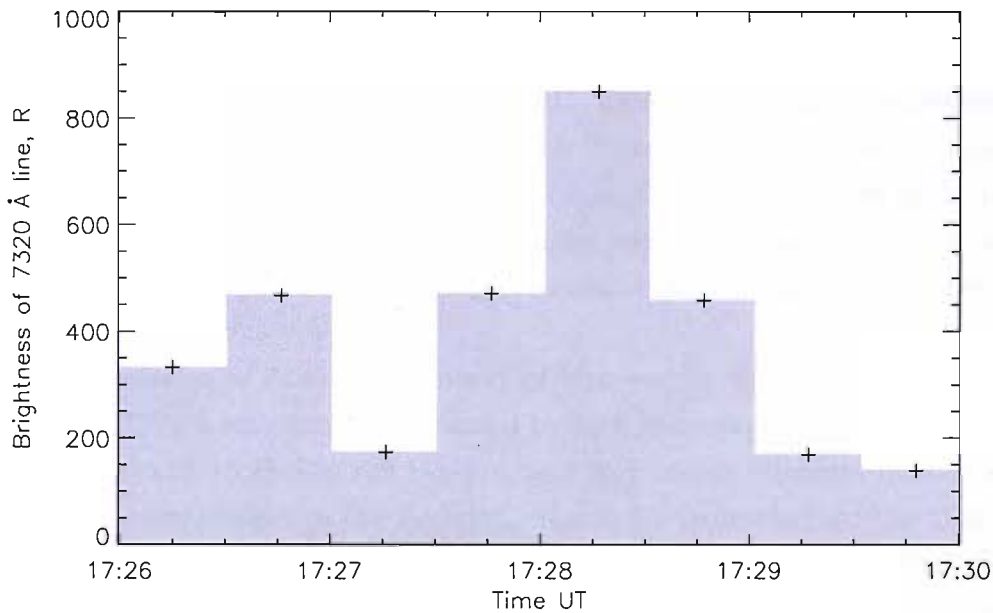

Figure 5.3: Brightness of 7320 Å O^+ emission line as measured by HiTIES for the period 17:26–17:30 UT. The bars show the entire exposure time of 30 s and each cross marks the central time of the exposure.

5.2 Photometer data

There is a significant advantage to using photometer data; it has a good temporal resolution, considerably better than that of both the spectrograph and the EISCAT Svalbard Radar.

The SIF photometer data for the period under study is shown in the bottom panel of figure 5.1. The 4861 Å and 4880 Å photometer plots are closely following the plot for the 5149 Å photometer. This suggests there is no proton precipitation during the event. The 4861 Å photometer measures the Hβ emission which comes from protons precipitation into the atmosphere, as well as galactic and geocoronal sources. This is Dopler-shifted towards the blue when observing proton precipitation from the ground, but is unshifted when observing the other sources [Galand et al., 2004]. The 4880 Å photometer provides a background for this measurement. It observes the N_2 Vegard-Kaplan (2,15) emission band which is present at a range of wavelengths close to the Hβ emission, with its band head at 4837 Å. In the presence of proton precipitation the 4861 Å photometer will record an increased brightness, whereas the 4880 Å photometer will not.

The emission at 5149 Å is a result of high energy electron precipitation, while the 7774 Å emission can be caused by both low energy electrons interacting with atomic oxygen in the F-region and high energy electrons interacting with molecular oxygen in the E-region. Figure 5.1 indicates that the 5149 Å and 7774 Å emissions behave differently over the time interval of the plot. This suggests that there is a significant low-energy component to the electron precipitation observed.

In order to evaluate changes in the low-energy precipitation more easily the ratio of intensities of 7774 Å to 5149 Å emissions has been calculated, and is plotted in the top panel of figure 5.4. At times when the ratio is high compared to the 7774 Å photometer intensity the photometers are observing aurora caused predominantly by low energy electron precipitation. This is the case for most of the timespan plotted in figure 5.4. At times when the ratio is low compared to the 7774 Å intensity the photometers are observing aurora with a significant high-energy component, such as between 17:27:45 UT and 17:28:45 UT. There are also two short high energy peaks close to 17:26:35 UT and 17:26:55 UT, but the high-energy component is less dominating at these times.

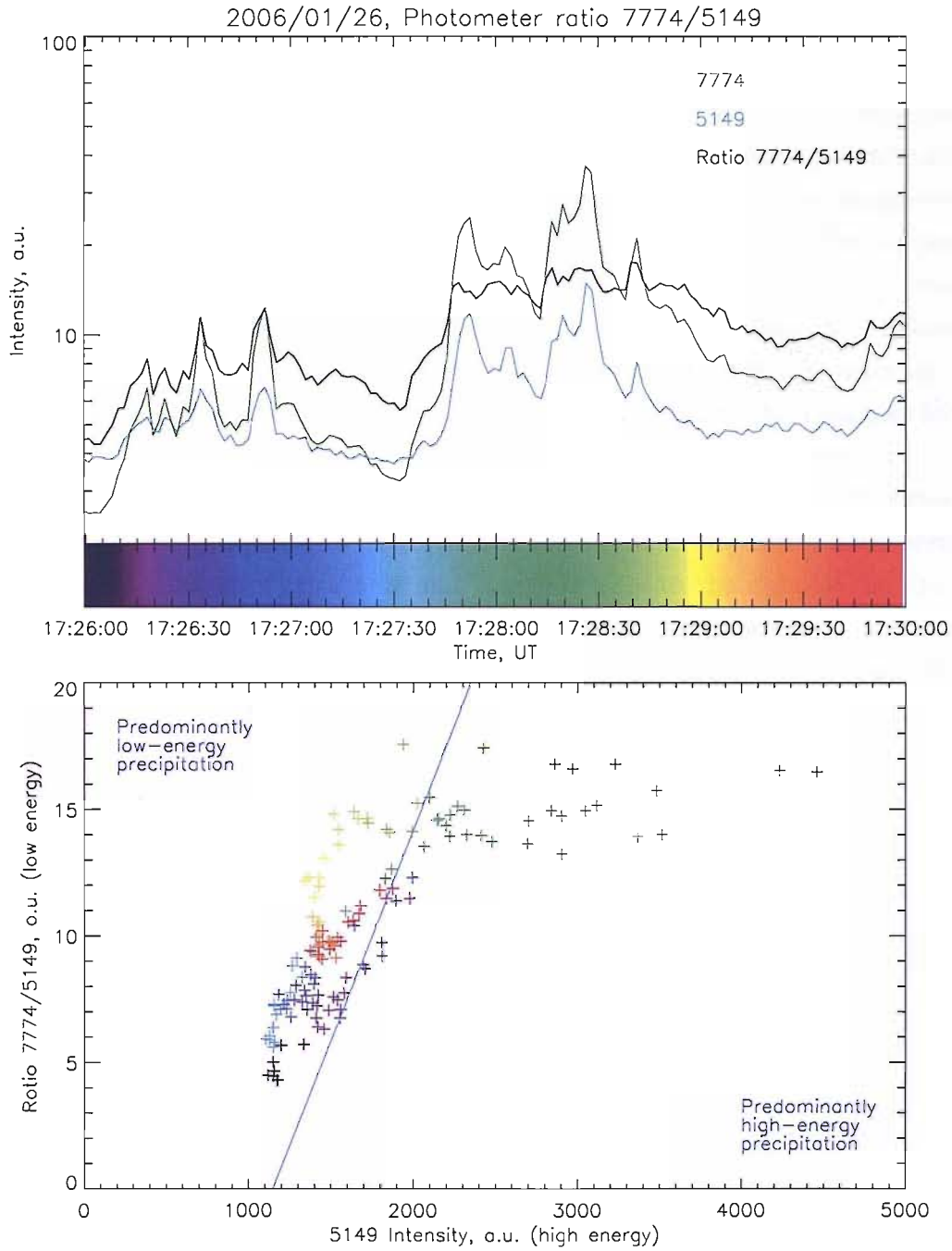

Figure 5.4: The ratio of intensities of the 7774 Å to 5149 Å SIF photometers, in the period 17:26–17:30 UT. This ratio is an indication of low energy electron precipitation. The photometers have not been intensity calibrated, but the 7774 Å and 5149 Å photometer data has been rescaled and is plotted here (top panel; green and blue lines respectively) for comparison. The scatter plot shown in the bottom panel highlights the characteristic energy of the electron precipitation.

The intensity measured by the 5149 Å photometer is also compared to the calculated photometer ratio with a scatter plot, shown in the bottom panel of figure 5.4. The high-energy component of the precipitation (5149 Å brightness) is on the x-axis, and the low-energy component (ratio 7774 Å : 5149 Å) is on the y-axis. All data for the time period 17:27–17:30 UT are plotted. Each cross represents one data point, where the photometer data has been integrated in time to 1.6 s temporal resolution in order to reduce noise. The crosses are coloured according to the time scale shown above the x-axis of the top panel. A line has been marked across the plot in blue to define two regions indicative of low and high energy precipitation. From this it is clear that low-energy precipitation dominates for a significant proportion of the 3 minutes for which data are plotted, whereas high-energy precipitation is observed only in certain periods, most strongly between 17:27:45 UT and 17:28:45 UT (green crosses). The two peaks at 17:26:35 UT and 17:26:55 UT can also be seen as a small number of dark blue and purple crosses to the right of the line. There are two prominent areas where the precipitation is especially dominated by low energy; shown in light green / yellow and light blue, corresponding to the periods 17:28:50–17:29:30 UT and 17:27:25–17:27:45 UT respectively. For periods where the crosses fall close to the blue line the precipitation is a mixture of high and low energies.

5.3 ESR data

Figure 5.5 shows data from the EISCAT Svalbard Radar 42 m dish for a relatively long period surrounding the event studied. The dish is fixed in the nominal field-aligned (zenith-pointing) position. At this time the radar was running the "Steffe" program, which has a temporal resolution of 6.4 s. However, the data shown in figure 5.5 has been integrated to 30 s resolution. Steffe has a lower limit on the range resolution of 1 km, but it is usually not this good as height integration of the data is required to obtain clear spectra which can be analysed.

In figure 5.5 there is a data gap between 17:15 UT and 17:27 UT, which is due to technical problems at the radar resulting in it not transmitting in this period. However, it is clear that there is a strong enhancement in the electron density just before 17:30 UT. There are also high electron and ion temperatures at this time, particularly when compared to later electron density enhancements at about 17:36 UT and 17:43 UT. High electron temperatures can indicate the presence of large field-aligned currents causing ohmic heating, as demonstrated by Lanchester et al. [2001] using EISCAT data, optical measurements and one-dimensional modelling of the auroral ionosphere. Large ion temperatures are known to be associated with increased electric fields orthogonal to the magnetic field, which form part of the current system between magnetosphere and ionosphere. Lanchester et al. [1996] used radar measurements of large ion temperatures to estimate the errors in radar trisatic velocity measurements, which were interpreted as large and variable electric fields close to auroral structures.

High resolution electron density data for the period analysed in chapter 4 are shown in figure 5.6, with the best possible time resolution obtainable with the ESR Steffe program. At this resolution it can be seen that at 17:27:30 UT the electron density peaks at high altitude, near 320 km. Shortly after this the density increases at low altitudes. This is consistent with the conclusions made from the HiTIES data; between 17:27 UT and 17:28 UT the observed aurora is caused by low energy precipitation (penetrating a relatively short distance into the ionosphere). Later higher energy precipitation causes an increase in electron density down in the E-region.

It is unfortunate that the radar was not running a few minutes earlier, at the very start of the auroral activity seen in the TLC data.

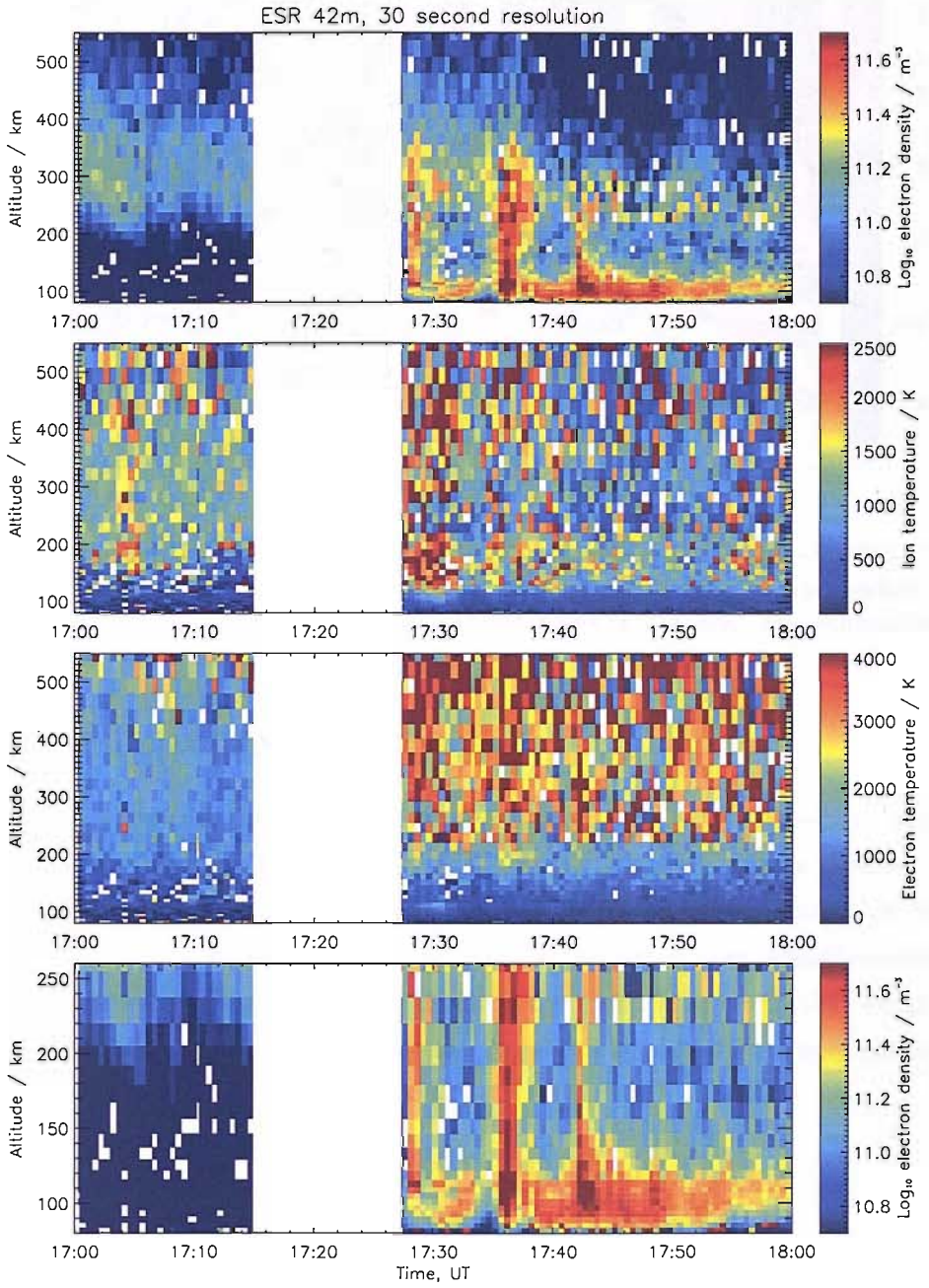

Figure 5.5: EISCAT Svalbard Radar (42 m dish) data for the event studied. The radar was experiencing technical difficulties between about 17:15 UT and 17:27 UT, resulting in the data gap. This data has been integrated in time to 30 s resolution.

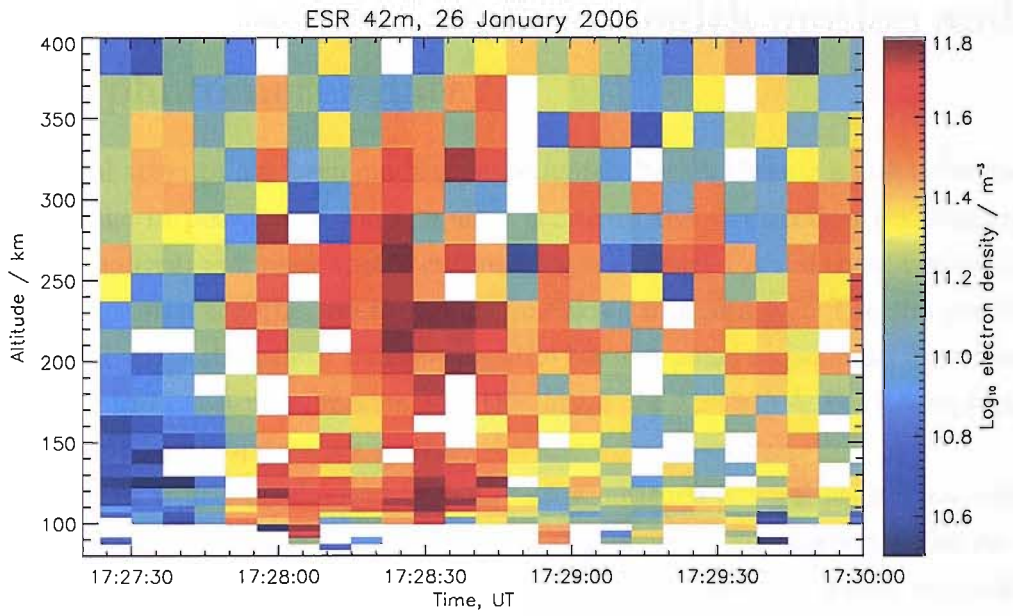

Figure 5.6: High resolution ESR 42 m data for the period 17:27:24–17:30:00 UT. Here only the electron density is shown. The main event studied in this thesis is the electron density peak at high altitude for the first 30 s of this plot. The enhancement is shown in yellow, above 300 km.

5.4 Summary of data

During this event all three of the instruments from which data have been shown in this chapter agree. From 17:27:30 UT until 17:27:45 UT they observe the effects of predominantly low-energy electron precipitation. After this they observe the effects of electron precipitation at higher energy, together with a continued low-energy component. Towards the end of the event the energy of the precipitation becomes lower again. No significant proton precipitation is observed.

5.5 Link between magnetic zenith motion and photometer data?

An initial attempt has been made to investigate whether there is a link between the change in position of the magnetic zenith in the y′ direction (exhibiting height changes) and photometer data during the event. Part of these two data sets are plotted together on the same time scale in figure 5.7. The top panel shows the magnetic zenith motions and the bottom panel shows data from the 5149 Å and 7774 Å photometers, and the ratio 7774 Å : 5149 Å. For a complete description of these data see sections 4.4 and 5.2 respectively.

Positive values of y′ could indicate a low altitude auroral zenith, caused by low altitude emissions resulting from high-energy precipitation. The opposite could also be true; negative values of y′ could indicate a high altitude auroral zenith caused by low-energy precipitaion. Photometer data will also show changes in the energy of precipitation. The 5149 Å photometer measures emission resulting from high-energy electron precipitation while the ratio 7774 Å : 5149 Å is a measure of low-energy precipitation.

Figure 5.7 shows there are two main peaks in photometer data in the time interval of the plot, centred at approximately 17:26:33 UT and 17:26:50 UT. At these times the ratio shown is relatively low compared to the 7774 Å photometer data, indicating an increase in high-energy precipitation relative to the low-energy precipitation. There are also two peaks in the zenith data, where the position in the y′ direction is more positive than in general throughout the plot, which again could be an indication of an increase in high-energy precipitation relative to low-energy precipitation. However, these two peaks appear to be centred at slightly different times to the photometer peaks; 17:26:32 UT and 17:26:46 UT. These discrepancies could be due to horizontal changes in the zenith position altering the shapes of the peaks resulting from altitude changes. Due to the limited amount of data no firm conclusions can be drawn from this, but the plot shows that a deeper investigation covering more events would be worth while.

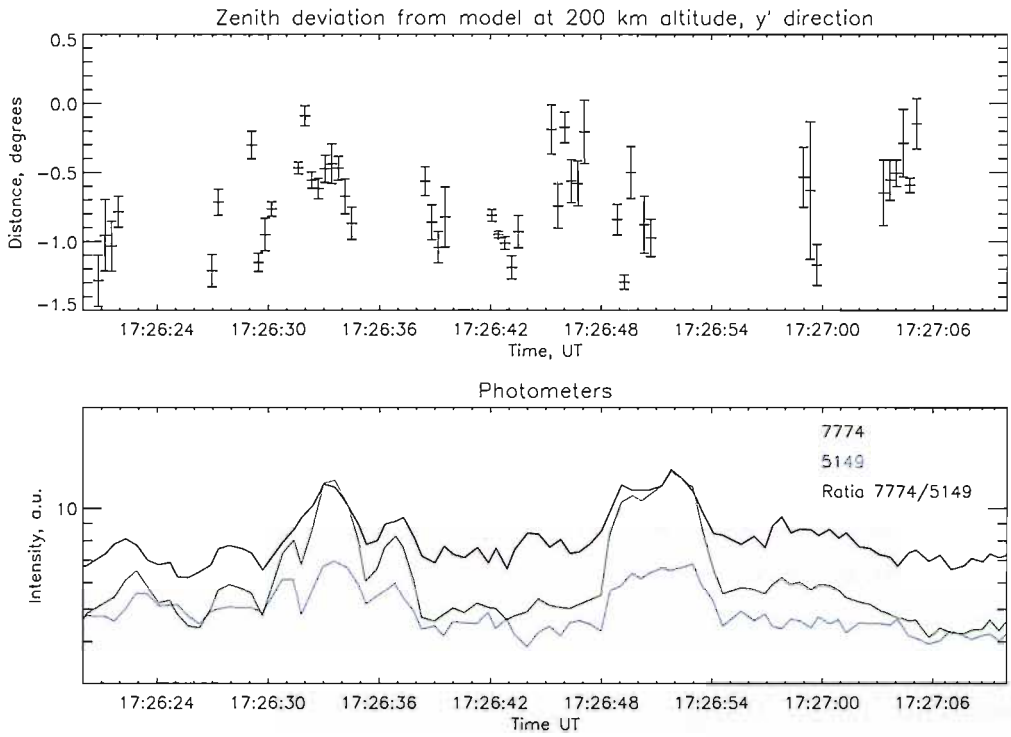

Figure 5.7: Zenith motion in the y′ direction (top panel, see section 4.4) and photometer data (bottom panel, see section 5.2) plotted on the same time scale. The photometer data here is shown at 0.4 s time resolution. With regards to the zenith motion variations in the y′ direction could be a result of emission height changes. Larger positive values of y′ could indicate emission at low altitude (high-energy precipitation). Larger negative values could indicate emission at high altitude (low-energy precipitation). The zero point corresponds to a magnetic zenith at 200 km altitude as found from the IGRF-10 magnetic field model. During the time period shown all points are negative.

Chapter 6

Modelling and Interpretation

6.1 The ion chemistry and electron transport model

A combined one-dimensional electron transport and ion chemistry model of the ionosphere has been developed over several years in Southampton. The electron transport part was developed at the University of Alaska by Lummerzheim [1987]. A short description of the combined model is provided here, but for a full explanation see the appendix in [Lanchester et al., 2001], and references therein.

A simple flow diagram of the model is shown in figure 6.1. The main inputs to the model are the MSIS-90 neutral atmosphere model [Hedin, 1991] and a time-varying electron precipitation energy flux. This precipitation is given as a total flux and peak energy for combinations of mono-energetic (represented by a Gaussian shape) and Maxwellian components. The model code combines these to create a single spectrum for each time step. As shown in figure 6.1 the output from the model is the density profiles of major ion species. It also gives ion production and loss rates, and the rates of the modelled ionospheric reactions, which can be used in the calculation of many auroral emissions.

At each time step the electron transport and ion chemistry parts of the model are carried out in turn. Starting at the highest altitude, the electron transport code calculates ionization rates, and the production and loss rates of the ion species. Secondary electrons produced here are considered, and feed into the electron transport model at the next height step. After this has been done for the entire height profile the ion chemistry code calculates reactions

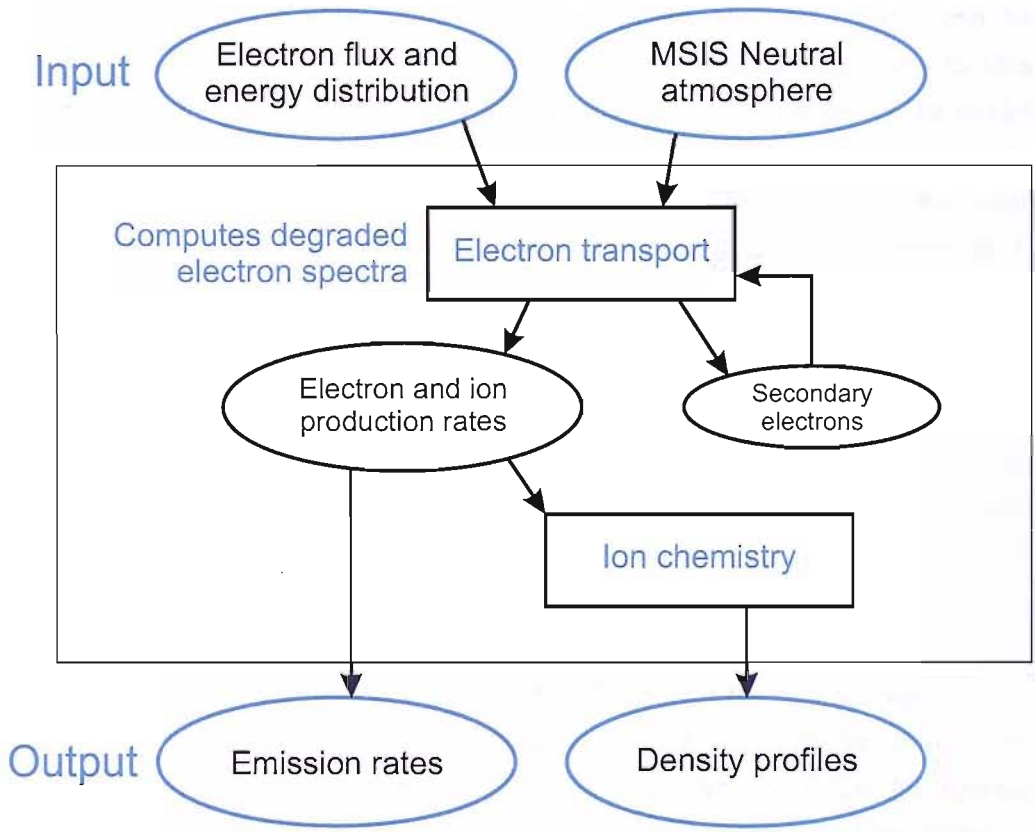

Figure 6.1: Flow diagram for the electron transport and ion chemistry model.

between the different species, again starting at the top and working down. This results in final density profiles for each species for a single time step. This resulting model ionosphere is then used in the next time iteration. The time step used in the model runs forming this work was 5×10^{-4} s, although the resulting ion production rates and density profiles are not written to the output file at this frequency.

The output ion production and loss rates, and the rates of the modelled chemical reactions, can be used in the calculation of emission brightnesses for comparison with instrument data. The model electron density can be compared with incoherent scatter radar data. The usual approach to this modelling is to vary the input electron precipitation until as many of the model results as possible agree with instrument measurements. This then allows the characteristics of the precipitation to be inferred, and conclusions to be made based on the similarities and differences between model and instrument data.

6.1.1 Calculating the model 7320 Å emission brightness

A method of calculating the 7320 Å emission brightness from the model output has been developed for this work, and for work involving the ASK (Auroral Structure and Kinetics) instrument (see [Ivchenko et al., 2008] for information about ASK). ASK uses a narrow passband spectral filter centred on the 7320 Å emission, but excluding the 7330 Å emission. Therefore the two halves of the 7320/7330 Å doublet must be modelled separately.

As explained in section 1.1.3, the 7320 Å emission is not prompt. It depends directly on the instantaneous density of $O^+(^2P)$ ions, rather than on the instantaneous electron flux or any reaction rate. This particular ion species is one of those for which the density profile is calculated by the model at each time step. Therefore the 7320 Å emission can be found by multiplying this density profile by a known rate coefficient. The emission profile is then integrated in height to obtain a total column brightness.

However, due to the multiplicity of $O^+(^2P)$, this is not completely straightforward. The 7320 Å emission is made up of two transition lines, one originating in the $^2P_{3/2}$ state and the other originating in the $^2P_{1/2}$ state. Therefore in order to calculate the brightness of the 7320 Å emission the densities of O^+ in these two states must be separated. The model only produces $O^+(^2P)$ without calculating the distribution among the total angular momentum states.

Wavelength (Å)	Transition	Einstein Transition Probability (s^{-1})
7329.9	$^2P_{1/2} - {}^2D_{3/2}$	$A_A = 9.39 \times 10^{-2}$
7330.7	$^2P_{3/2} - {}^2D_{3/2}$	$A_B = 5.78 \times 10^{-2}$
7318.6	$^2P_{1/2} - {}^2D_{5/2}$	$A_C = 5.63 \times 10^{-2}$
7319.4	$^2P_{3/2} - {}^2D_{5/2}$	$A_D = 1.07 \times 10^{-1}$

Table 6.1: Transitions making up the 7320/7330 Å doublet. Reproduced from [Dahlgren et al., 2008a], with Einstein transition probabilites from [Zeippen, 1987].

An equation has been derived to calculate the ratio of densities of $O^+(^2P_{1/2})$ to $O^+(^2P_{3/2})$ based on the ratio of brightnesses of the 7320 Å to 7330 Å emissions, as measured by the SIF spectrograph. This brightness ratio can be expressed as

$$R = \frac{B_{7320}}{B_{7330}} = \frac{A_C D_{1/2} + A_D D_{3/2}}{A_A D_{1/2} + A_B D_{3/2}} \tag{6.1}$$

where $B_{7320,7330}$ are the measured brightnesses of the 7320 Å and 7330 Å emissions, $A_{A,B,C,D}$ are Einstein transition probabilities as listed in table 6.1 and $D_{1/2,3/2}$ are the densities of O^+ in the $^2P_{1/2}$ and $^2P_{3/2}$ states. This equation can be rearranged to make the density ratio the subject:

$$\frac{D_{1/2}}{D_{3/2}} = \frac{RA_B - A_D}{A_C - RA_A} \tag{6.2}$$

This allows the density ratio to be calculated from HiTIES data, as the brightness ratio can be found from spectra measured in the O^+ mosaic filter panel. The density ratio can then be used to separate the model $O^+(^2P)$ density into the 1/2 and 3/2 total angular momentum states. The model 7320 Å emission brightness (in photons s^{-1}) is subsequently given by

$$M_{7320} = A_C D_{1/2} + A_D D_{3/2} \tag{6.3}$$

or in a more applicable form

$$M_{7320} = M_{den}\left[\frac{A_C R_{den} + A_D}{R_{den} + 1}\right] \tag{6.4}$$

where R_{den} is the density ratio $D_{1/2}/D_{3/2}$ and M_{den} is the modelled $O^+(^2P)$ density (total in both 1/2 and 3/2 total angular momentum states). The

factor in brackets is the rate coefficient for the 7320 Å emission. It would be interesting to see how this factor varies with time and struture of the aurora, but this work has not been done as part of this study.

Using the method outlined in section 5.1 the brightnesses of the 7320 Å and 7330 Å lines were found for the 30 s exposure beginning at 17:27:30 UT (the period modelled in this chapter). The brightness ratio was calculated as 1.39, leading to a density ratio of 0.359 and a rate coefficient for the 7320 Å emission of 9.36×10^{-2}.

6.2 Modelling the low-energy precipitation

Several attempts were made to model the 7320 Å emission brightness and the electron density at 17:27:30 UT, when low-energy precipitation dominated. This period is marked with a red line in figure 6.2, which shows data from both SIF and EISCAT on the same time scale for convenience. In this figure the top two panels show data from HiTIES; the 7320 Å emission brightness (top) and the complete spectra measured by HiTIES in the O^+ mosaic filter panel. The third panel of the figure shows the electron density as measured by the EISCAT radar and the last panel shows SIF photometer data.

The results of the most significant modelling tests are shown in figures 6.3–6.9. These figures have a common format, with the resulting electron density profiles and 7320 Å emission brightness shown in the top two panels and the input time-varying electron spectra shown in the bottom panel. The electron density profiles produced are compared with the EISCAT data for the event, and the calculated model 7320 Å emission is compared with the brightness of that line as observed by HiTIES.

Initially a Maxwellian shaped input spectrum was used, with a total flux of 1 mW/m^2. The peak energy changed from 300 eV to 100 eV, and then back to 300 eV again. The inital 300 eV flux was intended to "warm-up" the model ionosphere, creating ion and electron populations to approximate the start of the modelled period. The final 300 eV flux was intended to impose a finite lifetime on the high altitude electron density peak as measured by EISCAT, bringing the peak lower in altitude toward the end of the period. The results are shown in figure 6.3. The brightness of the model 7320 Å emission compares reasonably well with HiTIES, but is a factor 1.5 too small; the model produced

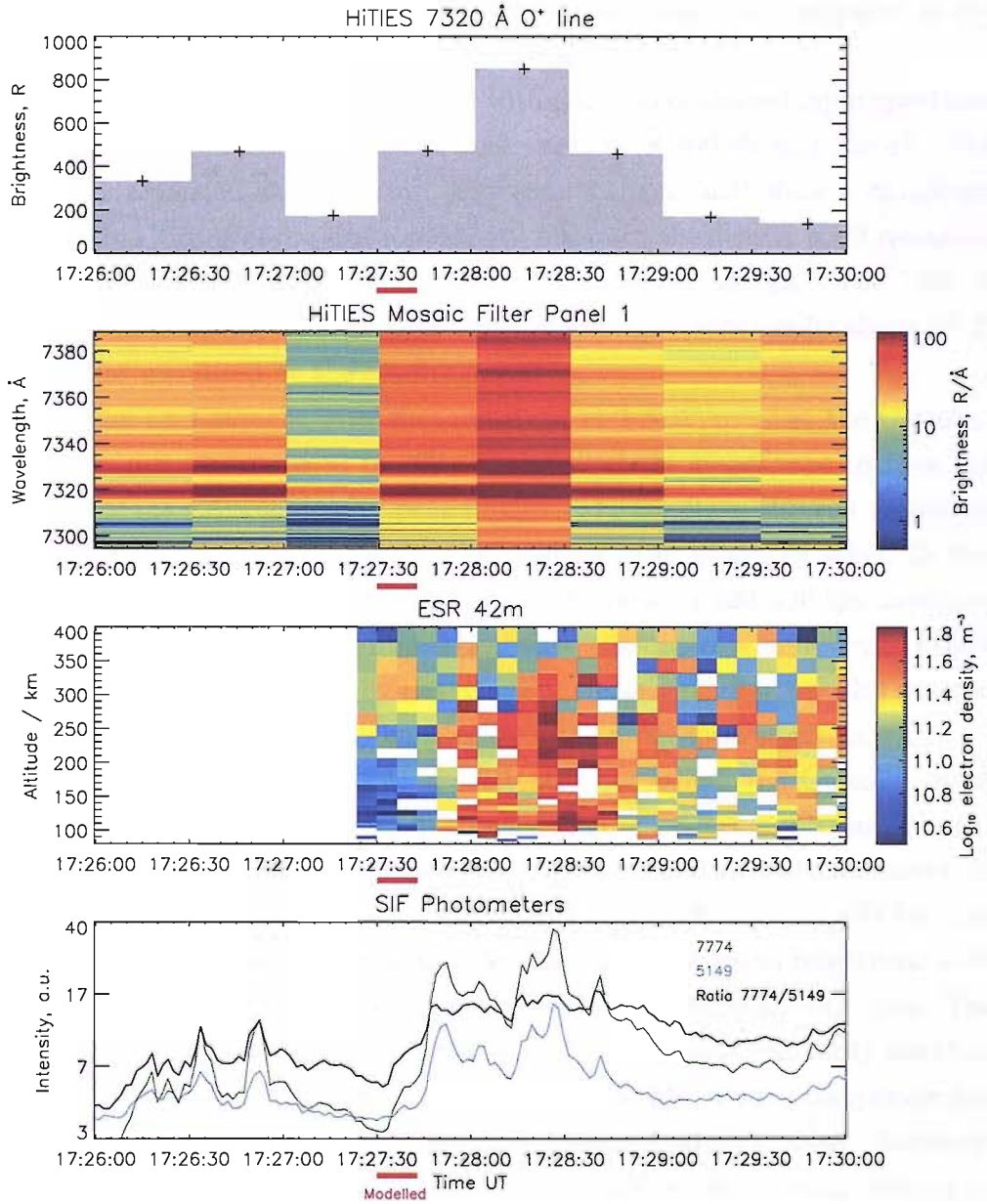

Figure 6.2: HiTIES (top two panels), ESR (third panel) and photometer (bottom panel) data for the period 17:26–17:30 UT. This is reproduced from figures (top–bottom) 5.3, 5.1, 5.6 and 5.4, and is shown here on the same time scale for convenience. The red line below each panel marks the time period modelled in section 6.2.

roughly 300 R compared with the 470 R measured by the spectrograph (see top panel of figure 6.2). However, the electon density is even less good. It is a factor of 10 too small and peaks at too low an altitude when compared to the EISCAT data (see bottom panel of figure 6.2).

For comparison the model was run with a Gaussian shaped input spectrum instead of Maxwellian, at the same peak energies of 300 eV and 100 eV. The total flux remained at 1 mW/m^2. The results (figure 6.4) show a significant increase in altitude of the electron density, although the density itself remained at approximately the same value as for the Maxwellian run. The 7320 Å emission brightness also increased considerably to a value only about 30 R above that measured by the spectrograph.

For the next run the total flux remained at 1 mW/m^2, but the Gaussian peak energies were reduced to 200 eV and 40 eV in an attempt to raise the altitude of the electron density peak further. The results of this run are shown in figure 6.5. The electron density peak did go up in height by about 10 km, but this is still approximately 70 km below the peak at 320–330 km measured by EISCAT. The 7320 Å brightness decreased slightly, to a value which agrees very well with that observed by HiTIES. The electron density was also reduced and so remained considerably smaller than the radar measurements.

The model was also run with a combined Maxwellian and Gaussian input spectrum, the results of which are shown in figure 6.6. This run has an input spectrum which is essentially the same as that used for the run shown in figure 6.5, but a Maxwellian component with a total flux of 0.2 mW/m^2 has been added. This has more than doubled the 7320 Å emission brightness, such that it is about 700 R larger than the value calculated from HiTIES data. The model electron density has also increased, but it remains significantly less than the EISCAT measured density. The addition of the Maxwellian component has caused the electron density to spread over a larger altitude range. However, the peak has remained at the same altitude, and so is not high enough to match the EISCAT electron density profiles.

As the altitude of the electron density peak was still too low, the model was run with a very low energy precipitation input of only 10 eV. This run is shown in figure 6.7. At these low energies the precipitating electrons are at the thermal level, so this run was a test of how such low energy electrons affect the output. It can be seen in the second panel that flux of such low peak energy produces negligible 7320 Å emission. There are two peaks caused by the

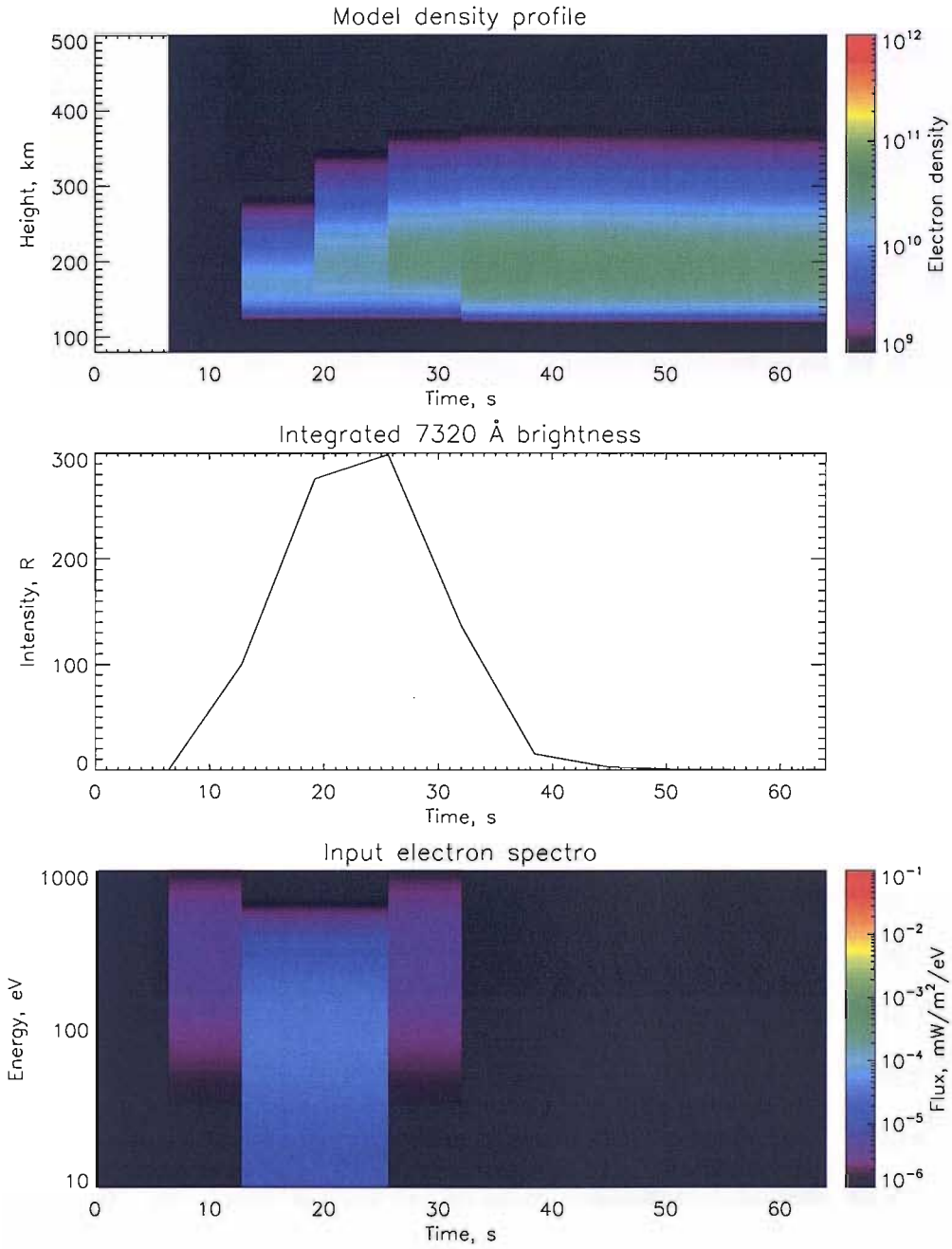

Figure 6.3: Here the model was run with a write-out timestep of 6.4 s. The input electron spectra used is Maxwellian in shape with a total flux of 1 mW/m^2. The peak energy is initially 300 eV, then drops to 100 eV before returning to 300 eV.

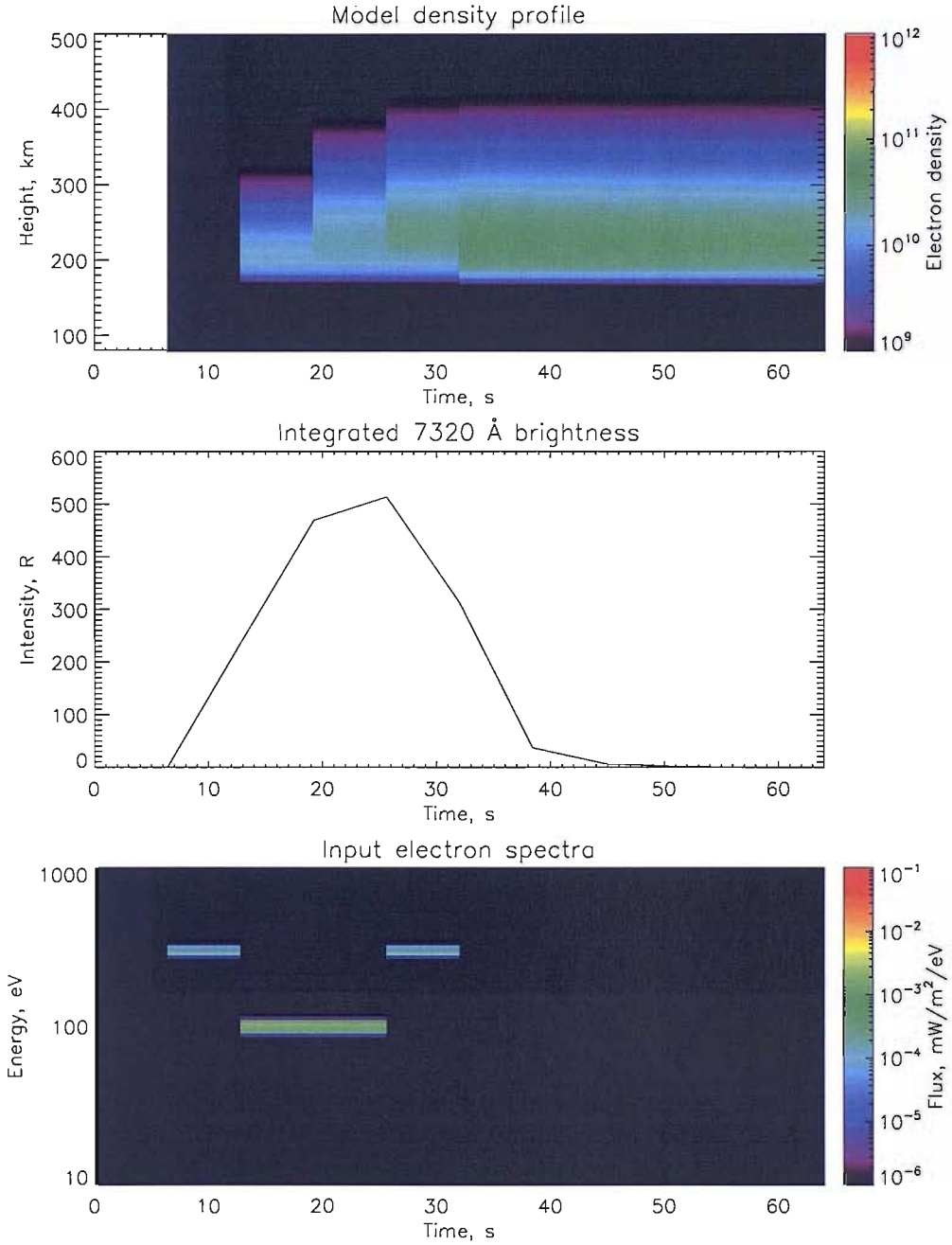

Figure 6.4: Model run as in figure 6.3 but with Gaussian input spectra instead of Maxwellian. Note the change in scale on the y-axis of the 7320 Å emission panel.

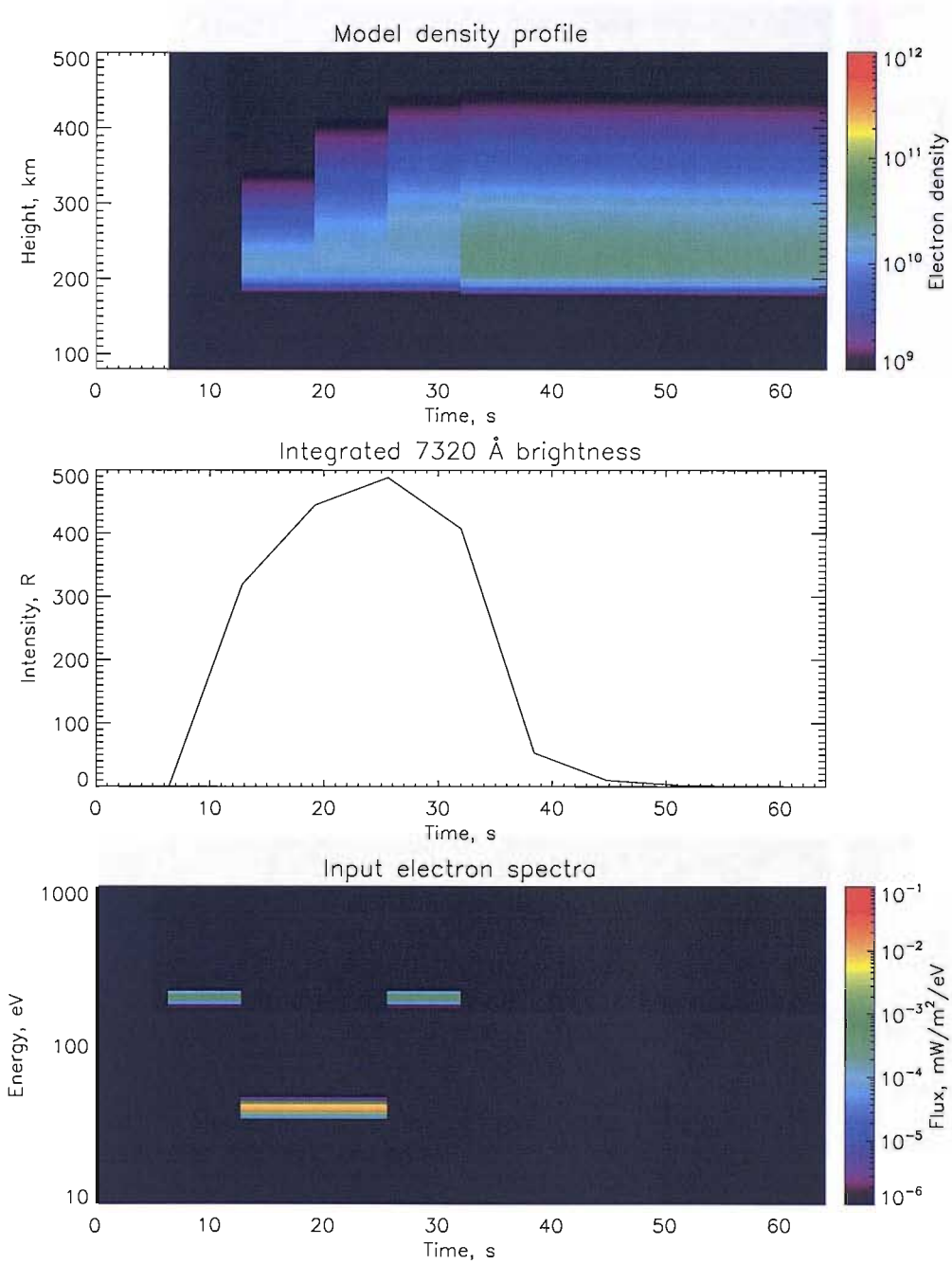

Figure 6.5: Model run with Gaussian input spectra as in figure 6.4, but with reduced peak energies of 200 eV and 40 eV.

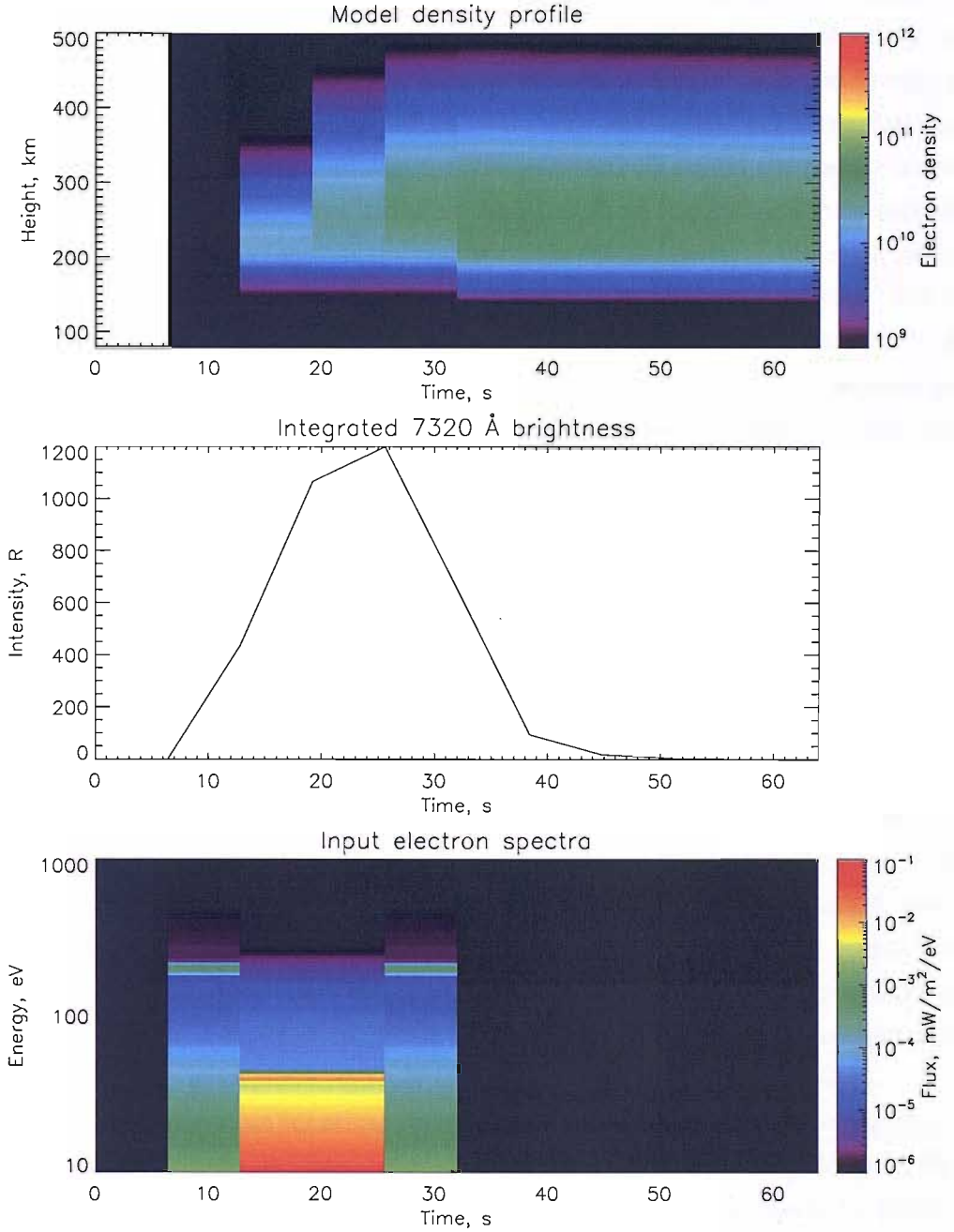

Figure 6.6: In this model run the input spectra were a combination of Gaussian and Maxwellian components, both at the same peak energies of 200 eV and 40 eV. The Gaussian component had a total flux of 1 mW/m^2 while the Maxwellian component had a total flux of 0.2 mW/m^2. A low-energy power law was added to the spectra such that the flux increased exponentially with decreasing energy below 20 eV.

200 eV input which appear identical in shape, suggesting the low-energy flux between them has no effect. The low energy input has also failed to produce any significant electron density at high altitude. Precipitation of electrons at this level appears to have little impact on the electron density in the F-region.

In order to model the effect of only the very low energy part, the flanking 200 eV flux periods were removed for the next run. Based on the results of the previous run the energy was increased to 20 eV, and the flux was increased to 7 mW/m^2 in order to increase the electron density. However, it was anticipated that this flux increase would result in a huge over-estimation of the 7320 Å brightness as observed by HiTIES. Previous runs indicated that the 7320 Å brightness subsides more quickly than the electron density in the absence of an input flux, as expected. After precipitation has ceased, no more $O^+(2p)$ ions are produced, and therefore the emission will fall off as the existing ions decay (with a lifetime of about 5 s). The electron density loss processes are much slower than this. In order to allow the electron density to increase to the level of the EISCAT data while limiting the 7320 Å intensity the input flux was pulsed. This may also be a more realistic simulation of rayed aurora moving in and out of the radar beam. The write-out timestep of the model was adjusted to provide model data at 0.64 s resolution, to assist in the analysis of the pulsed input. The results are shown in figure 6.8. This run was successful in keeping the 7320 Å emission reasonably low while continuing to build up the electron density. The altitude of the electron density peak was also higher than previous runs, at about 280 km, although the electron density was still too small when compared to EISCAT data, by a factor of about 10. The 7320 Å brightness agrees well with the value obtained from HiTIES, producing approximately 400 R. When compared to previous runs, this was the most successful in simulating the ionosphere at 17:27:30 UT, despite these discrepancies.

For comparison an identical run was carried out, but using an input spectrum with an increased peak energy (50 eV). The results are shown in figure 6.9. Both the electron density and 7320 Å brightness increased, by factors of approximately 8 and 4 respectively. When compared to the instrument data the model electron density was only slightly less than that measured by EISCAT, but the model 7320 Å brightness was about 400% of the value calculated from HiTIES data. The electron density peak dropped in altitude slightly from the previous run, and was about 50 km below the peak in the EISCAT data.

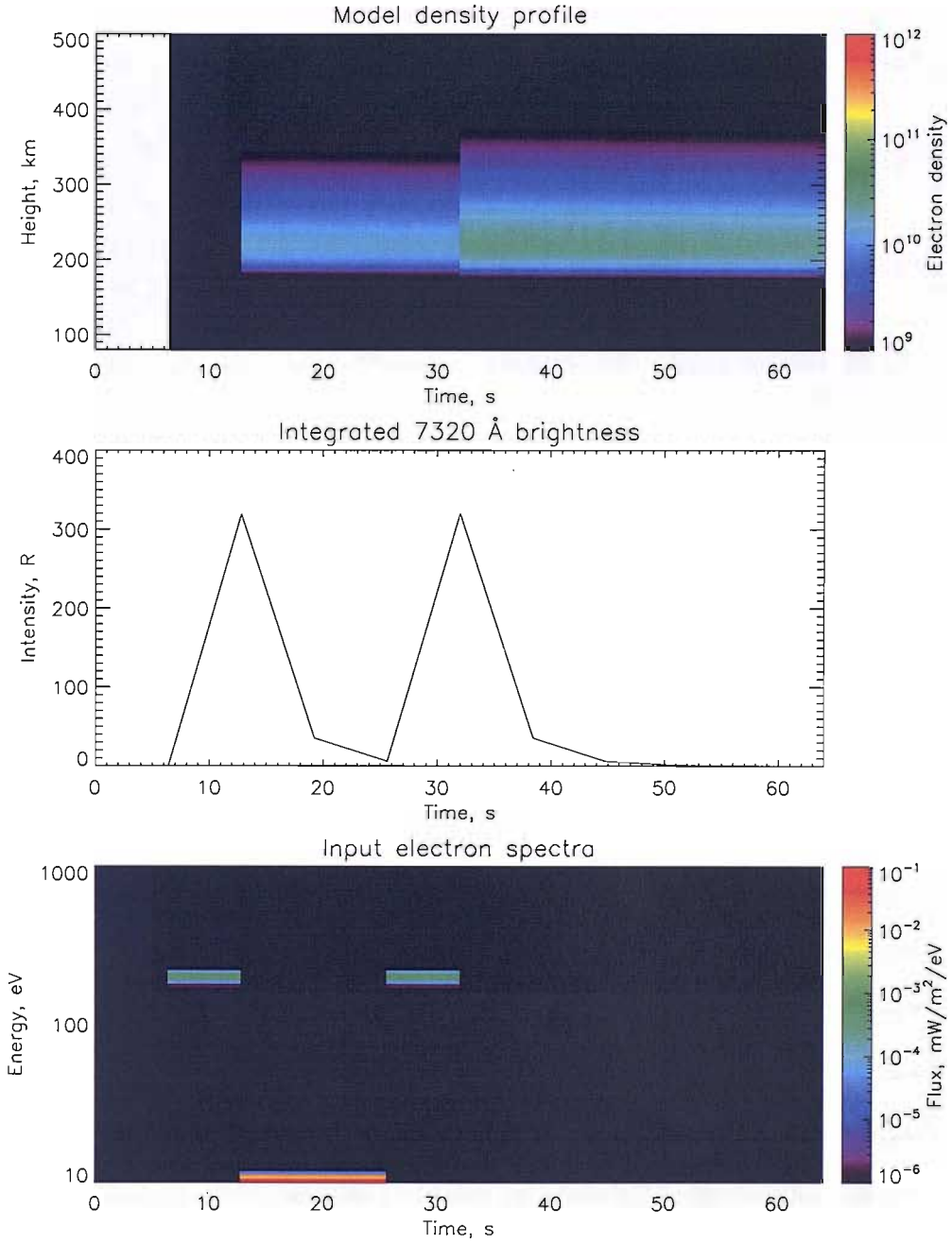

Figure 6.7: Here only a mono-energetic electron spectra is input to the model, at a total flux of 1 mW/m^2. In an attempt to create a high-altitude electron density peak a very low peak energy of 10 eV was used (sandwiched between fluxes with peak energies of 200 eV).

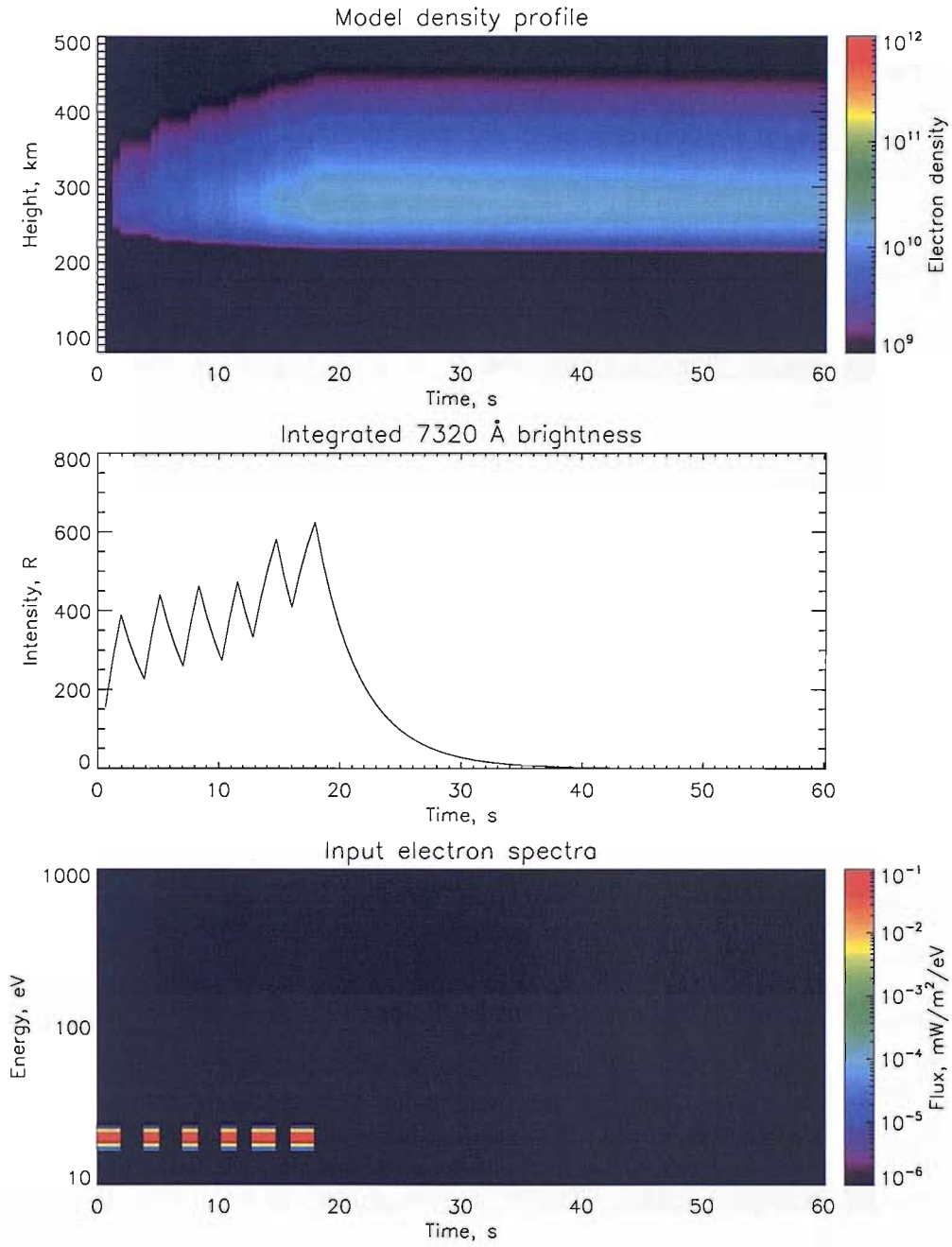

Figure 6.8: Model run with pulsed mono-energetic input spectra at 20 eV. The flux was 7 mW/m^2. Here the write-out rate of the model was increased by a factor of 10, such that the time resolution of this data is 0.64 s.

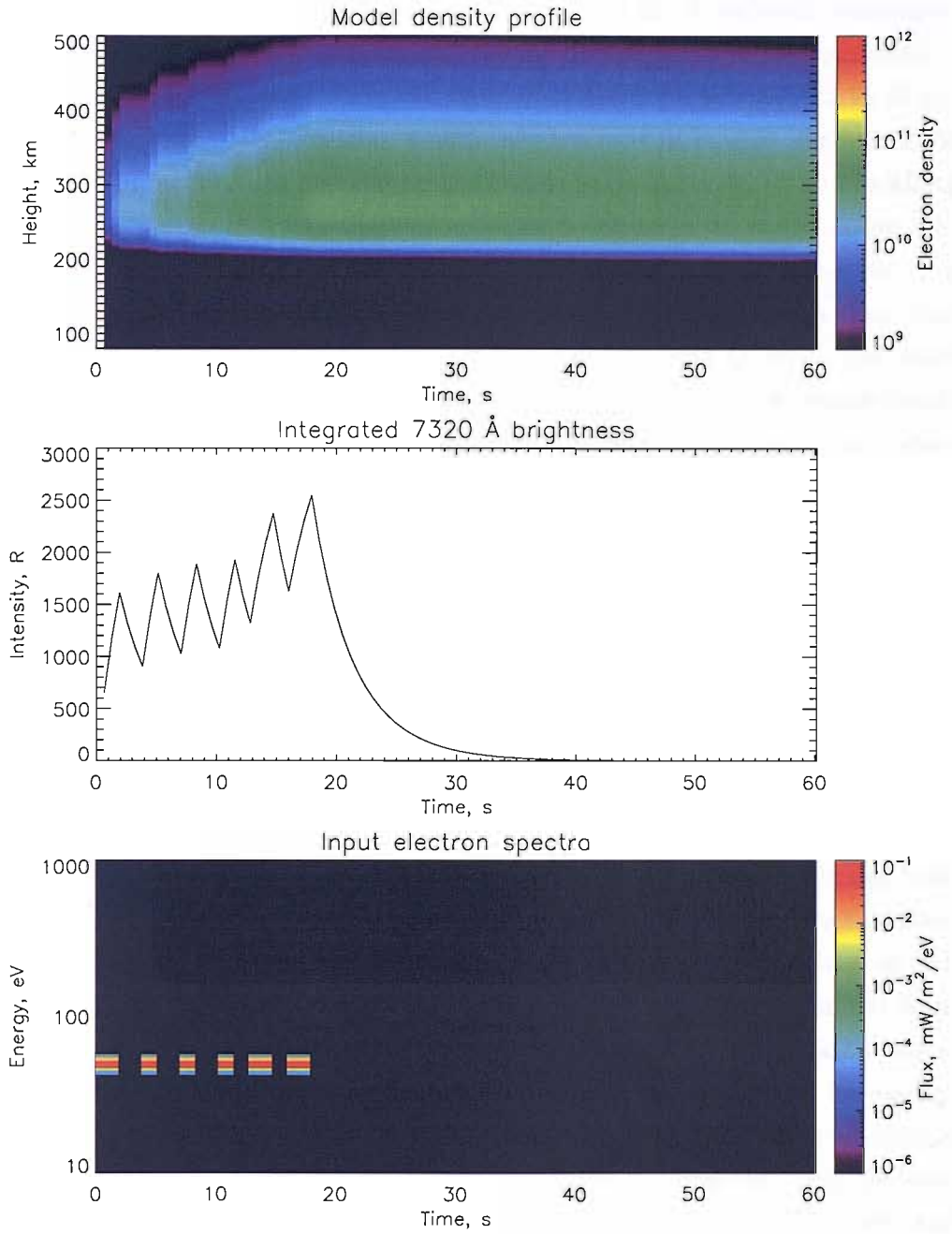

Figure 6.9: Model run as for figure 6.8 but with an increased peak energy of 50 eV.

6.3 Interpretation

To summarise the findings of the previous section, the model has been unable to simulate both the electron density profile and 7320 Å emission simultaneously. It has also failed to produce an electron density peak at the high altitude needed to match the EISCAT radar data. It is also noticable that in all of the model runs shown the electron density has reduced in magnitude very little after the input flux has been stopped. This is to be expected when modelling the ionosphere in only one dimension. Loss processes such as ionization and recombination cannot alone be responsible for a reduction in measured electron density at high altitude. The EISCAT data (see figure 6.2) shows that after 17:27:45 UT the high altitude electron density decreased quickly. The most likely explanation for this is that the electrons moved out of the radar beam. The model only simulates motions of electrons in one dimension (up and down the magnetic field line), so would not show this effect. Large ion temperatures measured by EISCAT at the time also support the argument that strong electric fields perpendicular to the magnetic field could be responsible for this motion perpendicular to the electric field. Similar conclusions were made by Lanchester et al. [1998], when comparing optical and radar data with model results.

The reason for the inability of the model to simulate successfully the low-energy precipitation observed becomes clear when considering the structure of the aurora in the magnetic zenith. Selected images from the TLC video data spanning the event are shown in figures 6.10 and 6.11. The image from 17:27:37 UT is shown in 6.11(a). In this image there are clear rays visible. However, there is very little aurora seen inside the radar beam (yellow circle). Based on the geometry of the magnetic field, the centre of a coronal form (such as in this image) comes from emission at high altitude, while the outer ends of the visible rays are at low altitude. This corresponds to low-energy precipitation close to the magnetic zenith and high-energy precipitation further out. When taking this into consideration it becomes clear that only the very low energy portions of the rays observed are within the EISCAT beam, and therefore when looking at the radar data it will appear as though the electron density peak is at high altitude. The enhanced electron density associated with the rays at lower altitudes is not in the radar field of view and therefore is not measured. This selection effect is demonstrated in figure 6.12. In running the

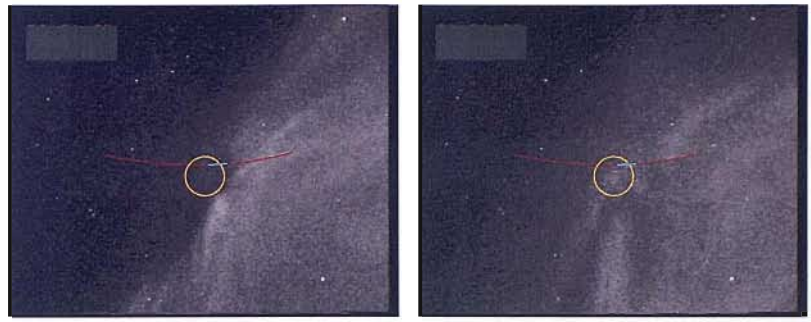

(a) 17:26:21 UT

(b) 17:26:33 UT

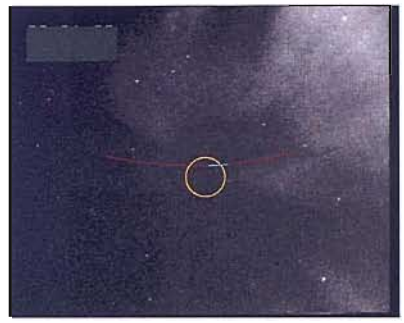

(c) 17:26:47 UT

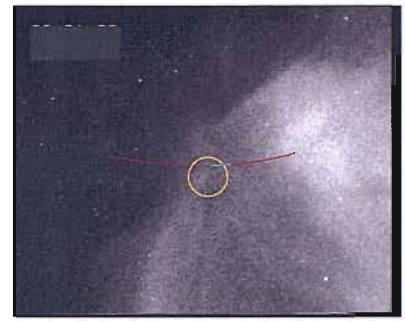

(d) 17:26:52 UT

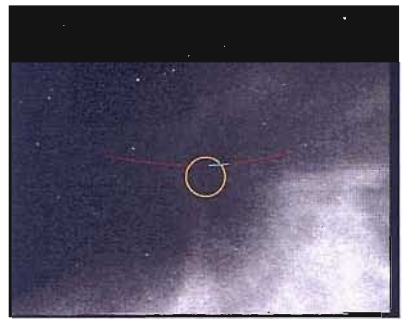

(e) 17:26:58 UT

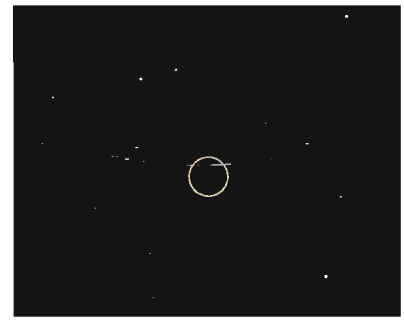

(f) 17:27:21 UT

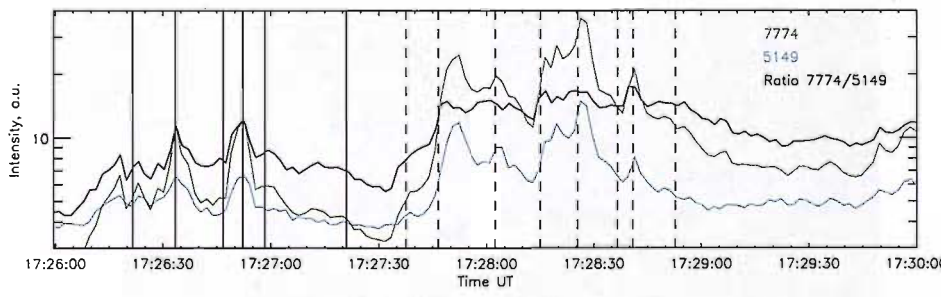

(g) Photometer data

Figure 6.10: TLC images for the first part of the event. The yellow circles mark the position and nominal size of the ESR beam. The red lines mark the position of the entire HiTIES slit, with the blue section highlighting the portion used when obtaining spectra from the O^+ panel. Photometer data (as in figure 5.4) are shown in (g). The vertical solid lines mark the times of the TLC images shown in this figure.

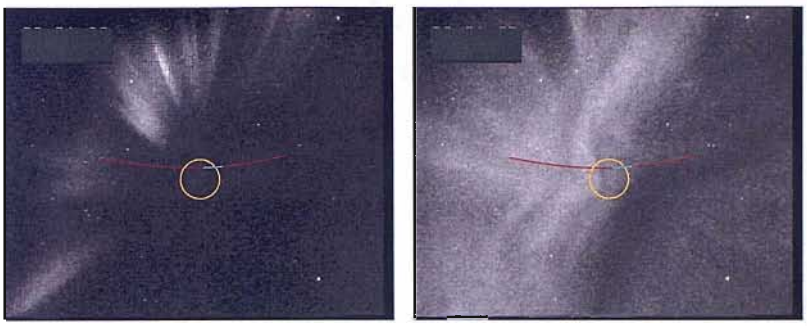

(a) 17:27:37 UT (b) 17:27:46 UT

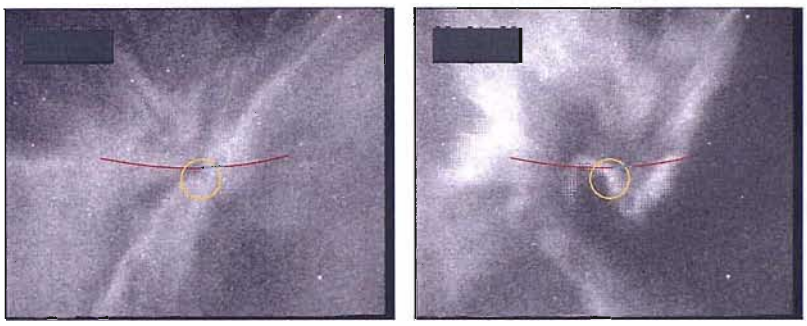

(c) 17:28:02 UT (d) 17:28:15 UT

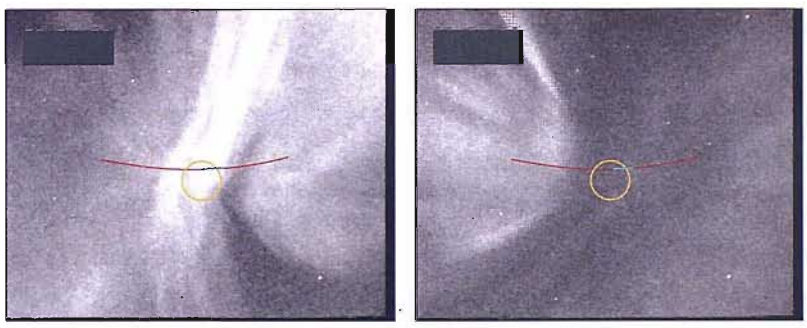

(e) 17:28:25 UT (f) 17:28:37 UT

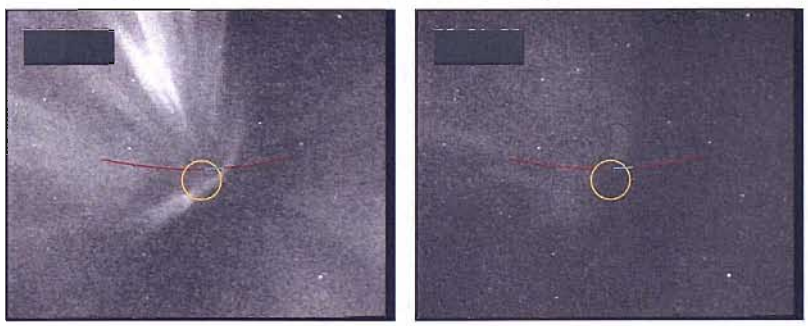

(g) 17:28:41 UT (h) 17:28:53 UT

Figure 6.11: TLC images for the latter part of the event. As in figure 6.10 the yellow circles and red/blue lines mark the position of the ESR beam and HiTIES slit respectively. The vertical dashed lines over the photometer data shown in figure 6.10(g) mark the times of the TLC images shown here.

model, it is assumed that the whole distribution is precipitating along one flux tube and it is not possible therefore to model only the tail of the distribution, which is what is being observed.

TLC images for the first part of the event are shown in figure 6.10. Note that there are no radar data for these times. For most of this period coronal forms are observed, with little aurora seen directly in the magnetic zenith. This explains why the photometer data suggest the precipitation is dominated by low energies (note that the photometers have a field of view of 1°, centred on the middle of the HiTIES slit). Images shown in figures 6.10(b) and 6.10(d) coincide with the two peaks seen in the photometer data. At these times there is aurora on the field line corresponding to the magnetic zenith, explaining the increased high-energy component. There is no aurora detectable in the TLC data in the period 17:27:20–17:27:30 UT, as seen in the example image shown in figure 6.10(f).

The latter part of the event, when radar data is available, is displayed in figure 6.11. Initially coronal rays are seen, corresponding to the low-energy precipitation inferred from the EISCAT, HiTIES and photometer data as explained earlier. The point where high-energy aurora clearly enters the ESR beam is shown in figure 6.11(b). Note the change in auroral form from corona to more varied and dynamic filaments and structures. There is an increase in low altitude electron density measured by EISCAT at 17:27:48 UT matching this image. An increase in the 5149 Å brightness (high-energy precipitation) measured by photometer also occurs, and the 7774/5149 Å photometer ratio reaches a maximum and levels-off at this point. Examples of the dynamic aurora following are shown in the next three sample images (figures 6.11(c)–6.11(e)). The lack of bright aurora in the magnetic zenith at 17:28:37 UT (figure 6.11(f)) matches a brief dip in 5149 Å brightness towards the end of the event, and the following peak is explained by the presence of short rays (short implies that they are almost parallel to the look-direction) in the magnetic zenith, as seen in figure 6.11(g). After this period of intense activity the aurora becomes more diffuse, as seen in figure 6.11(h) (c.f. no aurora in figure 6.10(f)). At this time EISCAT radar data show an electron density peak at approximately 260 km. On this occasion the peak is caused by precipitation on the field line which is entirely within the field of view of the radar beam, and is dominated by "true" low energy precipitation.

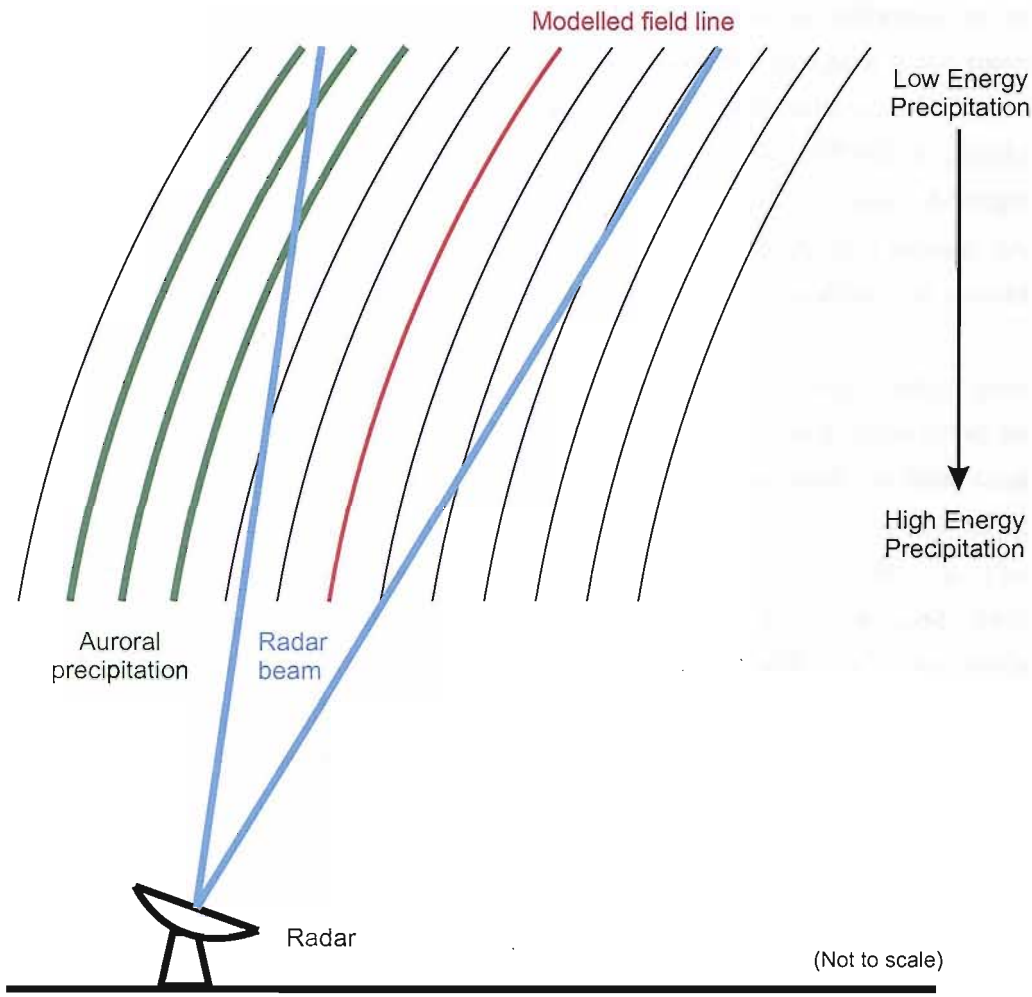

Figure 6.12: 2-dimensional diagram showing the ESR beam during coronal aurora. The thin grey lines represent magnetic field lines, and the green lines represent magnetic field lines with precipitation (and auroral emission) upon them. Low energy precipitation only reaches a relatively short distance down these lines, whereas high energy precipitation reaches low altitudes. The radar beam width is represented by the blue lines. From this geometry it is clear that only the top portion of the auroral emission (corresponding to low energy precipitation) will fall within the EISCAT beam. An example of the field line modelled with the ion chemsity and electron transport model is highlighted in red. This line lies totally within the radar field of view. Note that this diagram shows a slice through the ionosphere in two dimensions for illustrative purposes only. In reality auroral coronal forms are three dimensional, with low energy contributions on multiple parts of the radar beam perimeter.

When the TLC data is taken into account it is clear that it is impossible to obtain model results which successfully simulate the EISCAT data and HiTIES data at 17:27:30 UT simultaneously. EISCAT data gives no information on the lower parts of the active field lines, and therefore does not give a complete electron density profile for those field lines. The HiTIES data is also biased towards auroral activity at high altitude. This makes it very difficult to obtain a good approximation of the electron precipitation at that time. Another problem is that the HiTIES and ESR fields of view are not, and cannot be, identical. Therefore it is more difficult to compare their data when the aurora in that region is not approximately uniform.

It would be possible to model the ionosphere during the high energy precipitation in the period 17:28:00–17:28:30 UT, although consideration must be paid to the continued contribution to the EISCAT profiles made by field lines not entirely within the field of view. This could be taken into account using a result from the high altitude electron density observed at 17:27:30 UT. The effect of horizontal electric fields moving plasma in and out of the radar beam must also be considered as a limitation in 1-dimensional modelling. This study is on rayed aurora and its signatures, and so this modelling has not been done here, but it is a suggestion for future work and a continuation of this study.

Chapter 7

Conclusions

An auroral event which occurred in the period 17:25–17:30 UT on 26 January 2006 was studied in detail using the Spectrographic Imaging Facility and EISCAT Svalbard Radar, together with ionospheric modelling. The work concentrated mainly on auroral rays, particularly when in coronal forms. The event had relatively long periods of very clear coronal rays beneficial to this study, but also had periods of very dynamic aurora in the magnetic zenith, as well as periods of diffuse quiet aurora. This thesis has three main conclusions.

Firstly, in chapter 3, a new method for the intensity calibration of the HiTIES spectrograph using stars was explained and verified. This method has many advantages over using the calibration of the SIF flat-lamp directly, as has been done in the past. As stars are observed during a normal run a calibration can be obtained without substantial work in transporting the flat-lamp to an appropriately equiped lab and performing the calibration. This means a set of calibration coefficients can apply directly to a specific flat image, without relying on an intensity calibration made months or even years prior to the actual data acquisition. The star-based calibration will also take into account the transmission of the dome.

Secondly, in chapter 4, a method was shown for using camera data of coronal rayed aurora to find the actual position of the magnetic zenith to a good level of accuracy. Some techniques for analysing these data with the aid of a field model were also described, and it was shown that the magnetic zenith can move a considerable amount over very short periods of time (of the order 2° on timescales of a few seconds). It was also found that the zenith moves over angular distances larger than the nominal beam width of the ESR

42 m dish, and therefore will sometimes move outside of the beam. Motions of the magnetic zenith could not be determined completely as the altitude of the emissions is not known, and therefore changes in altitude and one horizontal dimension (y′) will appear the same in camera data.

Thirdly, chapter 6 highlighted the importance of considering contributions to radar-measured electron density from field lines which are not totally within the radar field of view. A method for calculating the ratio of densities of $O^+(^2P_{1/2})$ to $O^+(^2P_{3/2})$ and in turn modelling the 7320 Å auroral emission was shown in this chapter. This was used together with modelled electron densities to compare with HiTIES and EISCAT data. The results of this auroral modelling show that radar measurements will be biased towards high altitude electron density (low-energy precipitation), particularly when observing coronal rayed aurora.

One of the main results of this work has been the affirmation that it is highly important to consider the structure of the aurora when analysing ionospheric data. This shows how beneficial it is to use data from a variety of instruments simultaneously to study the same event. The work has also shown that it cannot be assumed that the EISCAT radar is continually pointing at the magnetic zenith at a constant height when in the "field-aligned" position. The auroral zenith has been shown to move outside of the main beam of the radar entirely for at least short periods of time on the occasion of the event studied here.

7.1 Future work

Some suggestions for the advancement of the work shown in this thesis are listed below:

- Model the high energy precipitation in the period 17:28:00–17:28:30 UT, and attempt to quantify the contribution from field lines not entirely within the field of view of the EISCAT beam using the results shown in this thesis.

- Apply the methods demonstrated here to more events. The 26 January 2006 event was chosen due to the very clear coronal rays present, before it was realised that the EISCAT data at this time was not complete. It would also be interesting to analyse systematically the magnetic

zenith motions in many events over a long period of time. Unfortunately the process as demonstrated in this work is quite time consuming due to the large human component involved, so it would also be advantageous to develop a faster more automated process.

- Find the emission height of coronal rays in order to compare altitude changes with changes in zenith position in the y′ direction (see chapter 4). Altitude variations could then be discounted from changes in y′, allowing the determination of zenith motions in all directions. There are several methods which could be used to obtain the height of coronal emissions. Two potential candidates are by triangulation from two or more separated cameras, or by using nitrogen rotational temperatures (see work by Jokiaho et al. [2008]).

- Study links between magnetic zenith motions and photometer data over several events (see section 5.5).

- Analyse the direction of the magnetic zenith from the centre of the ESR beam, as well as the radial distance.

- Compare ground magnetometer data with magnetic zenith motions.

- Intensity calibrate the photometer data, to compare with model results and to obtain a more accurate low energy component from the 7774 Å and 5149 Å photometers. A similar method to that shown in chapter 3 could be investigated.

- Use HiTIES to calculate the ratio of densities of $O^+(^2P_{1/2})$ to $O^+(^2P_{3/2})$ (see section 6.1.1) over a significant period of time, and study how the ratio changes with auroral structure, precipitation, time of day, and other such factors.

- Attempt to use model results (providing an estimate of the number of particles on a field line) together with the magnetic zenith motions calculated from video data to estimate field-aligned currents within the ionosphere. Results from this could be compared to satellite measurements, and also current estimates found from EISCAT data. If this proves successful then the method could provide estimates of currents at a higher time resolution than other instruments. Potential problems

could include the fact that total currents in the ionosphere are a result of motions of ions and electrons. Proton precipitation would also need to be considered, although this can be found from HiTIES data. Combining models of proton and electron precipitation is an important aim and would be a significant advancement of the ion chemistry and electron transport model used in this thesis.

Bibliography

C. W. Allen. *Astrophysical Quantities.* Athlone Press, London, third edition, 1973.

S. Chakrabarti, D. Pallamraju, J .Baumgardner, and J. Vaillancourt. HiTIES: A high throughput imaging echelle spectrograph for ground-based visible airglow and auroral studies. *Journal of Geophysical Research*, 106(A12): 30,337–30,348, 2001.

H. Dahlgren, N. Ivchenko, B. S. Lanchester, M. Ashrafi, D. K. Whiter, G. Marklund, and J. M. Sullivan. First direct optical observations of plasma flows in the metastable O^+ ion in discrete aurora. *Journal of Atmospheric and Solar Terrestrial Physics*, 2008a. In preparation.

H. Dahlgren, N. Ivchenko, B. S. Lanchester, J. Sullivan, D. Whiter, G. Marklund, and A. Strømme. Using spectral characteristics to interpret auroral imaging in the 731.9 nm O^+ line. *Annales Geophysicae*, 2008b. In preparation.

H. Dahlgren, N. Ivchenko, J. Sullivan, B. S. Lanchester, G. Marklund, and D. Whiter. Morphology and dynamics of aurora at fine scale: first results from the ask instrument. *Annales Geophysicae*, 2007. In press.

M. Galand, J. Baumgardner, D. Pallamraju, S. Chakrabarti, U. P. Løvhaug, D. Lummerzheim, B. S. Lanchester, and M. H. Rees. Spectral imaging of proton aurora and twilight at tromsø, norway. *Journal of Geophysical Research*, 109:A07305, 2004.

A. E. Hedin. Extension of the msis thermosphere model into the middle and lower atmosphere. *Journal of Geophysical Research*, 96:1159–1172, 1991.

D. M. Hunten, F. E. Roach, and J. W. Chamberlain. A photometric unit for the airglow and aurora. *Journal of Atmospheric and Terrestrial Physics*, 8 (6):345–346, 1956.

N. Ivchenko, E. M. Blixt, and B. S. Lanchester. Multispectral observations of auroral rays and curls. *Geophysical Research Letters*, 32:L18106, 2005.

N. Ivchenko, B. S. Lanchester, J. Höök, M. Bampton, H. Dahlgren, D. Whiter, A. Strømme, and Y. Ivanov. Auroral Structure and Kinetics - A new optical instrument for auroral studies. *Journal of Applied Remote Sensing*, 2008. In preparation.

O. Jokiaho, B. S. Lanchester, N. Ivchenko, G. J. Daniell, L. C. H. Miller, and D. Lummerzheim. Rotational temperature of N_2^+ (0,2) ions from spectrographic measurements used to infer the energy of precipitation in different auroral forms and compared with radar measurements. *Annales Geophysicae*, 2008. In press.

Margaret G. Kivelson and Christopher T. Russell, editors. *Introduction to Space Physics*. Cambridge University Press, 1995.

B. S. Lanchester. *Relation between discrete auroral forms and magnetic field disturbances*. PhD thesis, University of Southampton, 1985.

B. S. Lanchester, K. Kaila, and I. W. McCrea. Relationship between large horizontal electric fields and auroral arc elements. *Journal of Geophysical Research*, 101(A3):5075–5084, 1996.

B. S. Lanchester, M. H. Rees, D. Lummerzheim, A. Otto, K. J. F. Sedgemore-Schulthess, H. Zhu, and I. W. McCrea. Ohmic heating as evidence for strong field-aligned currents in filamentary aurora. *Journal of Geophysical Research*, 106(A2):1785–1794, 2001.

B. S. Lanchester, M. H. Rees, K. J. F. Sedgemore, J. R. Palmer, H. U. Frey, and K. U. Kaila. Ionospheric response to variable electric fields in small-scale auroral strutures. *Annales Geophysicae*, 16:1343–1354, 1998.

D. Lummerzheim. *Electron transport and optical emissions in the aurora*. PhD thesis, Univ. of Alaska, Fairbanks, 1987.

I. W. McCrea, M. Lester, T. R. Robinson, J.-P. St.-Maurice, N. M. Wade, and T. B. Jones. Derivation of the ion temperature partition coefficient $\beta_{\|}$ from the study of ion frictional heating events. *Journal of Geophysical Research*, 98(A9):15,701–15,715, 1993.

I. McWhirter, I. Furniss, B. S. Lanchester, S. C. Robertson, J. Baumgardner, and M. Mendillo. A new spectrograph platform for auroral studies in Svalbard. In K. U. Kaila, J. R. T. Jussila, and H. Holma, editors, *Proceedings of 28th Annual Optical Meeting*, Sodankylä Geophysical Observatory Publications 92, pages 73–76, Sodankylä, Finland, 2003.

Yu. Ralchenko, A. E. Kramida, J. Reader, and NIST ASD Team. NIST atomic spectra database (version 3.1.4), [online], 2008. Available at: http://physics.nist.gov/asd3 [2008, February]. National Institute of Standards and Technology, Gaithersburg, MD.

M. H. Rees. *Physics and chemistry of the upper atmosphere.* Cambridge University Press, 1989.

M. H. Rees, V. J. Abreu, and P. B. Hays. The production efficiency of $O^+(^2p)$ ions by auroral electron impact ionization. *Journal of Geophysical Research*, 87(A5):3612–3616, 1982.

M. H. Rees, R. A. Jones, and J. C. G. Walker. The influence of field-aligned currents on auroral electron temperatures. *Planet. Space Sci.*, 19:313–325, 1971.

H. Rishbeth. EISCAT. In *Proceedings of Esrange Symposium, Ajaccio, 24–29 April 1978*, ESA SP-135, pages 85–94, Noordwijk, 1978. ESA Publ. Div.

F. Sigernes, J. M. Holmes, M. Dyrland, D. A. Lorentzen, S. A. Chernous, T. Svenø, J. Moen, and C. S. Deehr. Absolute calibration of optical devices with a small field of view. *Journal of Optical Technology*, 74:669–674, 2007.

A. Vallance Jones. *Aurora.* D. Reidel Publishing Company, Dordrecht-Holland/Boston-U.S.A., 1974.

V. A. Velichko, N. E. Molochushkin, V. P. Samsonov, and S. R. Smotritskiy. The orientation of rays with a short lifetime in the active corona of polar aurorae. *Geomagnetism and Aeronomy*, 25(5):729–731, 1985.

M. Wedlund. Airglow OH(8,3) rotational temperatures Svalbard (78°N) 2003. Master's thesis, Royal Institute of Technology (KTH), Sweden, 2007.

C. J. Zeippen. Improved radiative transition probabilities for O II forbidden lines. *Astron. Astrophys.*, 173:410–414, 1987.